Marine Micropaleontology 186 (2024) 102323

Contents lists available at ScienceDirect

Marine Micropaleontology

journal homepage: www.elsevier.com/locate/marmicro

Origins and paleoclimatic and paleoceanographic significance of laminated sediments of middle Pleistocene age from the southern Bering Sea

Jonaotaro Onodera [a,*], Alan E.S. Kemp [b], Richard B. Pearce [b], Keiji Horikawa [c], Kozo Takahashi [d]

[a] Research Institute for Global Change, Japan Agency for Marine-Earth Science and Technology, Japan
[b] National Oceanography Centre, University of Southampton, United Kingdom
[c] Faculty of Science, Academic Assembly, University of Toyama, Japan
[d] Department of Earth & Planetary Sciences, Graduate School of Sciences, Kyushu University, Japan

ARTICLE INFO

Keywords:
Varve
Diatom
Rare earth element
Sinking particle flux
Bering Sea
Pleistocene

ABSTRACT

Laminated diatomaceous sediments occur intermittently in the Bering Sea over the past 5 million years. A varve (annually deposited) origin for the laminae has been suggested, but there is currently no consensus. Here, we report results of a study of two laminated intervals dating from ~528 ka and ~ 782 ka from IODP Site U1340 on the Bowers Ridge. We combine conventional micropaleontological methods with scanning electron microscope analysis that resolves the seasonal cycle of flux events recorded and demonstrates an annual origin for the laminae. Resting spores of *Chaetoceros* spp., and more rarely of *Thalassiosira antarctica* represent early spring blooms with the latter likely due to increased meltwater input. Diatom laminae containing concentrations of *Shionodiscus trifultus*, *Thalassiosira* spp., *Actinocyclus curvulatus*, and *Neodenticula seminae*, represent flux from the main spring-summer bloom episodes, with the latter indicating influx of seed populations from the North Pacific Alaskan Stream. Concentrations of *Coscinodiscus* spp. in the uppermost part of the diatom laminae represent "Fall Dump" sedimentation of these stratified-adapted diatoms in response to break down of summer stratification in autumn/early-winter storms. The lithogenic laminae represent mainly winter deposition and rare earth element analysis suggests provenance from the southern Bering Sea shelf and the Aleutian Arc. Productivity was high in the studied intervals with total mass fluxes around 5 times higher than modern values. Variation in lamina thickness and diatom composition contain periodicities of 2–8 years, as well as a bi-decadal variability likely related to influence of the Pacific Decadal Oscillation.

1. Introduction

The Bering Sea contains one of the world's most productive marine ecosystems, driven by intense algal blooms fueled by abundant nutrient supplies mainly from the sub-surface water column along the shelf-slope (e.g., Mizobata et al., 2002). Primary productivity in the Bering Sea is dominated by spring and summer blooms of the dominant phytoplankton, primarily diatom algae. The annual cycle of primary production has been monitored by sampling of the surface ocean and by sediment trap studies. Sediment traps have demonstrated seasonal pulses of flux, with major diatom flux in the spring and summer and terrigenous flux, primarily in the winter months (Takahashi et al., 2002; Takahashi et al., 2000). Sedimentary records of such flux events have the potential to record seasonal to interannual variability, where the sedimentary record is undisturbed by bioturbation. Such records occur most often in marginal marine settings where reduced oxygenation has limited benthic activity allowing individual flux events to be preserved as sedimentary laminae (Schimmelmann et al., 2016).

Intervals of laminated sediment are, in fact, a frequent occurrence in the Bering Sea sequences. Research on piston cores has recorded laminated intervals within the warm intervals of Bølling Allerød and in the earliest Holocene (Caissie et al., 2010, Cook et al., 2005, Kuehn et al., 2014). IODP coring has demonstrated their intermittent occurrence throughout the past 5 Ma (Takahashi et al., 2011; Schlung et al., 2013; Knudson and Ravelo, 2015; Cassie et al., 2016; Kender et al., 2019). Palaeotemperature records of the last 90 ka indicate that earlier laminated intervals also coincided with warm, interstadial episodes where elevated productivity and flux led to benthic anoxia and water column denitrification (Schlung et al., 2013). The Bering Sea laminated intervals correlate with widely recurrent intervals elsewhere in the circum-Pacific

* Corresponding author.
E-mail address: onoderaj@jamstec.go.jp (J. Onodera).

https://doi.org/10.1016/j.marmicro.2023.102323
Received 15 August 2023; Received in revised form 8 December 2023; Accepted 8 December 2023
Available online 14 December 2023

including the Santa Barbara Basin (Caissie et al., 2010; Cook et al., 2005) and Baja California margin (Cartapanis et al., 2014). Initial explanations for the laminated intervals called on teleconnections with Greenland and/or changes in intermediate water ventilation (Kuehn et al., 2014; Schmittner et al., 2007). However, an emerging consensus proposes that the reduced oxygen conditions responsible for laminae preservation originate in the warming associated with interglacial or intermediate climates (Knudson et al., 2021; Praetorius et al., 2015). In this explanation, a combination of physiologically enhanced plankton growth driven by warming, together with iron fertilization from flooded continental shelves drove increased productivity. The increased productivity and flux led to reduced bottom water oxygenation, inhibiting benthic activity leading to the preservation of laminated sediment.

Previous studies of the Bering Sea laminated sediments have produced conflicting views on their origins. While sediment description and sampling and X-radiography have shown these to be couplets of diatom-rich and lithogenic sediment-rich laminae (Katsuki et al., 2014; Kuehn et al., 2014), there has been no consensus as to their seasonal origin. Based on bulk sedimentation rates for an interval spanning the Bølling through early Holocene, Cook et al. (2005) proposed an annual origin, but Caissie et al. (2010) working on the same interval in a different core argued that bulk sedimentation rates were too low to support an annual origin. Others have assumed an annual occurrence since it fits with the modern flux cycle (Katsuki et al., 2014, Kuehn et al., 2014).

Our purpose in this contribution is to examine two laminated intervals recovered from IODP Site U1340 on the Bowers Ridge (Fig. 1). A combination of conventional sampling and detailed Back Scattered Electron Imagery (BSEI) of resin-embedded sediment is used to delineate and characterize individual flux events. In this way we clarify the significance of individual, often near-monospecific, diatom laminae and use these to reconstruct the annual cycle of production and flux and to inform palaeo-reconstructions.

2. Oceanographic setting and paleoceanographic context

In the modern Bering Sea, the exchange of sea surface water between the North Pacific and the Bering Sea occurs via the Kamchatka Strait and several passages between the islands of the Aleutian arc (Fig. 1a). The Alaskan Stream, the greatest source of surface water flow into the Bering Sea, enters the basin through the Aleutian Arc and flows eastward, forming the Aleutian North Slope Current (ANSC). The ANSC turns northwestward near shelf edge, forming the Bering Slope Current (BSC), the primary current responsible for exchange with the continental shelves (Stabeno et al., 1999). The water partially flows out to the Arctic Ocean via the Bering Strait (the modern water depth ~ 50 m). However, the shallow depths of the sill would have limited water exchange during periods of low sea-level.

The vertical distribution of dissolved oxygen concentration in the Aleutian Basin shows that oxycline (strongest vertical gradient) lies between 300 and 600 m depth (Panteleev et al., 2013) (Fig. 1b). The

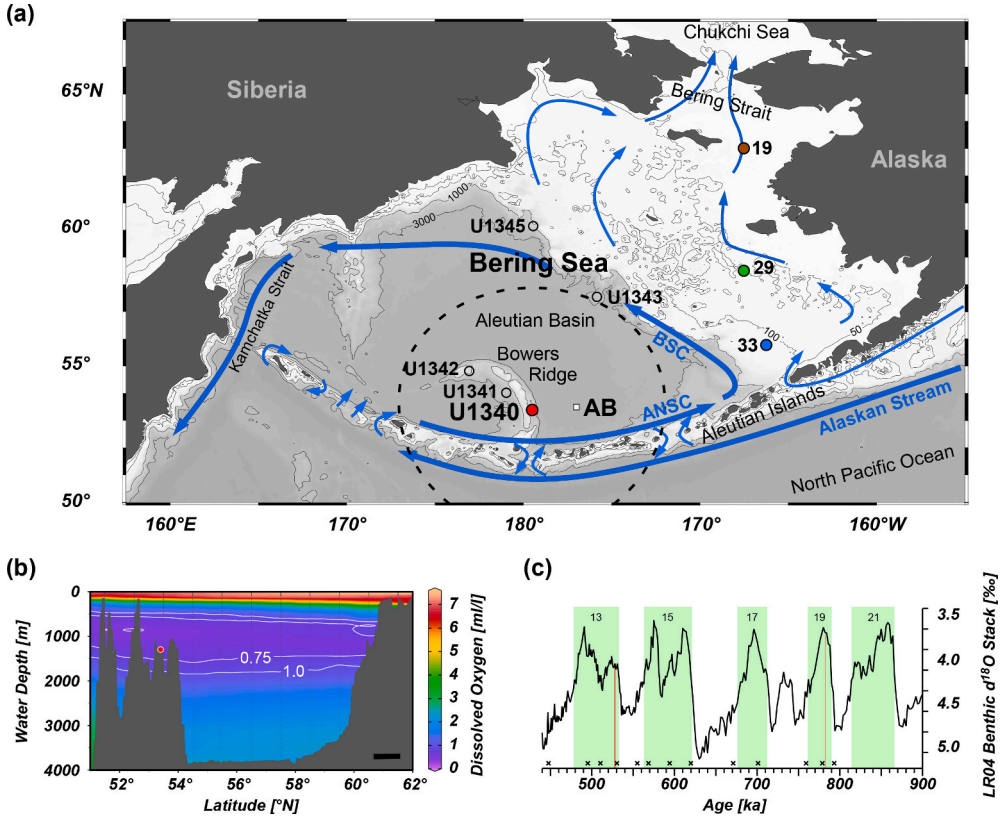

Fig. 1. Bathymetry map, climatological distribution of dissolved oxygen concentration in the Bering Sea, and the relationship of studied sample age and benthic $d^{18}O$ stack curve. (a) bathymetry map with four depth contours (50, 100, 1000, and 3000 m depth) based on the geographic data "The GEBCO_2014 Grid", version 20,150,318, www.gebco.net. The directions of surface currents are indicated. Abbreviations: ASNC: Aleutian North Slope Current; BSC: Bering Slope Current. The circular symbol in red is the drilling position of the studied core samples. The open circular symbol is the drilling position of IODP Exp. 323 mentioned in this paper. The rectangular symbol is the position of sediment trap mooring Station AB. The circular symbols in blue, green, and brown over the shelf are the position of referenced coring sites of Asahara et al. (2012) for REE analysis. The circular dash line is a distance of 500 km from the studied Site U1340. (b) Climatological distribution of dissolved oxygen concentration based on World Ocean Atlas 2013 (Garcia et al., 2014) along longitudinal Section in 179.5E-178.5 W. The bar shows the horizontal distance of 100 km. (c) The stack curve of benthic foraminifer $\delta^{18}O$ (Lisiecki and Raymo, 2005) with the age position of studied laminated samples (shown in red line). The shade in green represents interglacial MIS periods. The cross symbols represent the estimated age of the magnetic susceptibility events "CHI-O" to "CHO-CC" (Lund et al., 2016). (For interpretation of the references to colour in this figure legend, the reader is referred to the web version of this article.)

oxygen minimum zone with the lowest dissolved oxygen of ~0.5 mL/L is around 600–1200 m depth in the central Aleutian Basin for modern conditions (Roden, 1995; Panteleev et al., 2013). The radiolarian assemblage in sediment cores from different depths (884–3182 m) in the Aleutian Basin shows a change in vertical water mass structures for the late Pleistocene (Tanaka and Takahashi, 2005). Millennial and glacial-interglacial changes in the condition of minimum dissolved-oxygen concentration and vertical migration/expansion on the lower limit of the oxygen minimum layer are the important keys to forming discontinuous varve sediments at the core site on the Bowers Ridge, as the same as shown in laminated sediments along the shelf-slope of Bering Sea (e.g., Schlung et al., 2013; Kuehn et al., 2014). Expansion of the oxygen minimum zone is one of the key processes of ocean carbon cycling (Baroni et al., 2020).

As a high latitude marginal sea with connections to both the North Pacific and Arctic Oceans, the Bering Sea is a key influence on both local and global ocean and climate change (Kender et al., 2018; Okazaki et al., 2010). For example, flow of low salinity Bering Sea waters to the Arctic Ocean may have preconditioned the climate system for late Pliocene global cooling (Horikawa et al., 2015). Enhanced North Pacific Intermediate Water (NPIW) formation during glacial restriction of Bering Sea outflow may have influenced the global meridional overturning circulation (Knudson and Ravelo, 2015). Furthermore, in the Pleistocene, sea ice formation in the Bering Sea is thought to have acted as a control on glacial NPIW formation (Detlef et al., 2018). The monitoring of such changes in sea ice extent is aided by the use of diatom indicators (Cook et al., 2005).

Diatoms are dominant phytoplankton in the Bering Sea, and their production and settlement in the ocean interior are one of the important processes of biogeochemical cycles (Takahashi et al., 2000, 2002). In the modern Bering Sea, interannual variation of primary production significantly reflects a change in hydrographic conditions such as sea surface temperature and sea ice condition (e.g., Brown et al., 2011). Decadal monitoring of settling particle flux in the Bering Sea shows diatom dominance in the trapped sinking particles and interannual variation of sinking particle flux and the particle contents (Takahashi et al., 2000, 2002, Onodera and Takahashi, 2009). Diatom microfossil assemblages had been applied in many paleoceanographic studies (e.g., Sancetta et al., 1985; Katsuki and Takahashi, 2005; Cassie et al., 2016). The biogeography of diatom assemblage in the Bering Sea approximately corresponds to hydrographic variations (e.g., Sancetta, 1982; Ren et al., 2014), and the relationships between diatom distribution and climatic hydrographic conditions can be applied for micropaleontological paleoceanographic studies. Because diatoms are the main contributors to sinking particles in the Bering Sea, it is expected that annual variation in diatom accumulation rate and assemblage identified in sediment laminae will reflect past hydrographic conditions and the background environments on annual to decadal time scales.

2.1. Materials

Based on the sediment core description of IODP Expedition 323 in the Bering Sea (Takahashi et al., 2011), the core samples with the clear laminated structure were chosen from the Lithologic Unit I of Hole IODP323-U1340A (53°24.0008′N 179°31.2973′W, 1294.7 m water depth; Expedition 323 Scientists, 2011) located on the eastern slope of the Bowers Ridge just under the oxygen minimum layer (Fig. 1a, b). Lithologic Unit I is characterized by alternating layers of diatom ooze and diatom silt. At least 37 sediment beddings of laminated (<1 cm) structure was recorded in the visual core description for the Lithologic Unit I at this hole (Takahashi et al., 2011). After the observation and check of lamination quality, slab-shape samples for this study were taken from the core intervals 10H-1 W (136-149 cm), 10H-2 (1-16 cm), and 14H-1 W (60-75 cm and 73-88 cm) at the Kochi Core Center, Japan, using the sampling method of Pike and Kemp (1996). The ages of studied sediments are estimated as around ~528 ka and ~782 ka for Sections 10H and 14H, respectively, based on the correlation of magnetic susceptibility events with Site U1343 where benthic foraminiferal oxygen isotope stratigraphy was established (Takahashi et al., 2011; Asahi et al., 2016; Lund et al., 2016). The studied laminated sediment from Section 14H-1 corresponds to the early period of Marine Isotope Stage (MIS) 19, and that of 10H-1 and 10H-2 to the early MIS 13 (weak warming phase) (Fig. 1). The sea level for ~782 ka was around 20 m lower than the modern level (Batchelor et al., 2019), while the sea level for the sample of Section 10H in the early MIS 13 was around −50 m lower (Batchelor et al., 2019). The depth of ~50 m is nearly the deepest level of the Bering Strait, and the shallower area of the eastern Bering Sea shelf was probably land. Therefore, the climate condition, coastal configuration, and hydrographic conditions at the core site were different between the two studied sample periods.

3. Methods

3.1. Sediment preparation and diatom analysis

The sample slabs taken at the Kochi Core Center were sent to the National Oceanography Center, Southampton, and the X-radiograph images of sediment slab pieces were taken (Fig. 2a). Off-cuts of the slab sample were embedded in epoxy resin using the methods of Pike and Kemp (1996). Polished thin sections (PTS) of the embedded sediment cut perpendicular to the laminae were made for observation using back-scattered SEM images (BSEI) (Fig. 2b, c). Photo-mosaics of entire thin sections were made by assembling BSEI using Adobe Photoshop (Fig. 2c). The thickness of sediment lamination was measured as the mean of five measurements for each layer on the BSEI mosaic (Fig. 2c). Past settling particle flux was tentatively estimated from the mean thickness of annual laminations (varve) and dry bulk density, using the value of 0.37 g cm^{-3} measured from the diatomaceous laminated sediment at Site U1342-4H-5, 29-31 cm (Takahashi et al., 2011). BSEI with further high magnification were taken from the top to bottom of each thin section (Fig. 2d) in order to identify the dominant diatom types in each lamina (Fig. 3). On the available remains of the sample slab including homogeneous sediment just below the laminated sediment, mm-scale subsamples of sediment pieces (Fig. 2e) were taken for BSEI topographic imagery (Fig. 4).

Cross-sections of diatom frustules and the diatom valves in thin-section BSEI (Fig. 3) were counted for each lamina. The detailed BSEI of polished thin sections (PTS) (Fig. 2d, 3) shows that there are some distinctive cross-sections of diatom frustules/valves, so that identification of a range of different taxa is possible. The diatom observation in detail in BSEI of PTS was conducted by morphologically categorizing encountered diatom cross-sections into 12 groups based on diatom observation in smear slides (below) and in the topographic BSEI of subsamples (Fig. 4; Table 1). Among major diatoms in the studied samples, the genera *Actinocyclus* spp., *Shionodiscus* spp., and *Thalassiosira* spp. (except for *T. antarctica* resting spores) could not be readily distinguished from each other in BSEI cross section and were treated as a "discoidal" group. The category of "setae" refers mainly to the setae of *Chaetoceros* spp. although the similar spine-like structures of other diatom frustules might be included. The BSEI PTS counts assess the diatom cross sections that comprise the cross-section area of the lamina. This is distinct from the diatom assemblage in the smear slide (see discussion below).

To provide a more detailed taxonomic analysis, conventional optical microscopy was also undertaken on smear slides of sediment subsamples. The samples taken for smear slides generally included a number of laminae since individual laminae were too thin to sub-sample. Smear slides for diatom assemblage analysis (one slide for each subsample) were prepared with the Mountmedia of Fujifilm Wako Pure Chemical Corporation (refractive index = ~1.5) as a mountant. Encountered diatom valves remaining 1/2 whole form were identified at genus or species level at x1000 magnification. To estimate the diatom

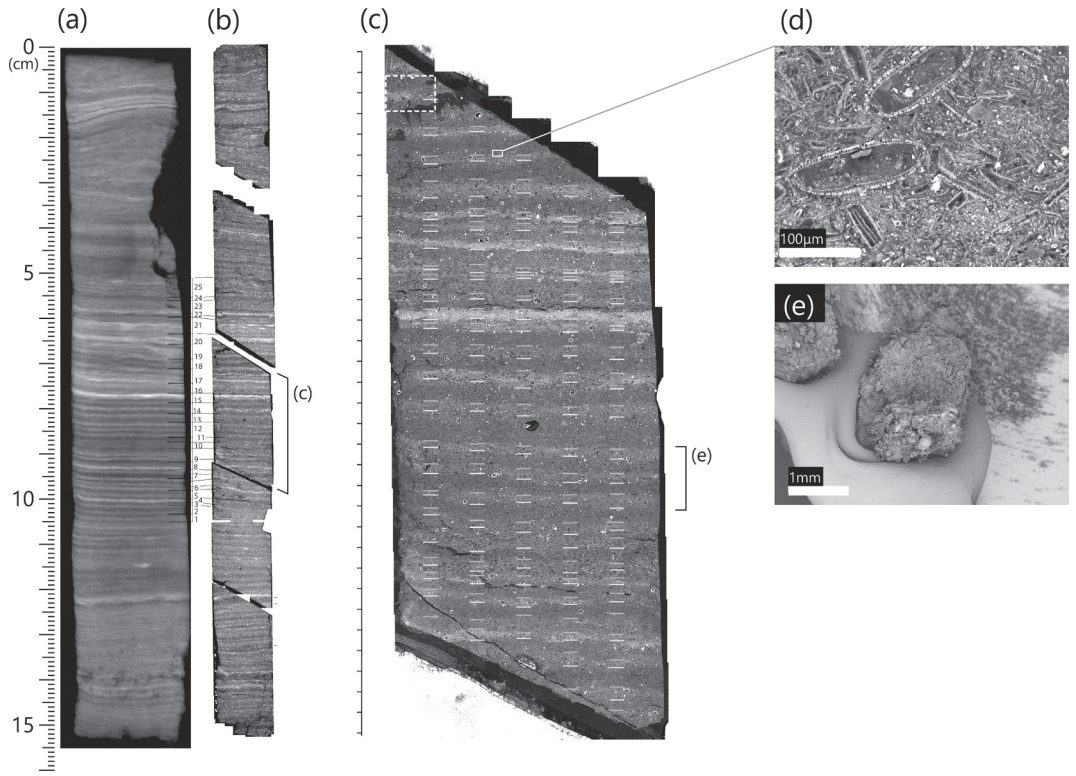

Fig. 2. Applied back-scattered SEM image (BSEI) observation. (a) taking soft-X ray photograph on the sediment sample slab of U1340A-10H-1 W, 134-149 cm. (b) preparation of thin sections and the correspondence of lamination with the original sediment slab (a). (c) making a compiled mosaic of enlarged BSEIs (dashed box size) over the thin section with five columns of short lines showing identified lamination boundaries to measure lamina thickness. (d) taking detail BSEI from the top to bottom of the thin section to observe the dominant diatom type in each lamina. (e) subsampling of a few mm thick sediments along with lamination, and the BSEI. The small lines and numbers between (a) and (b) show the boundary and ID of subsamples.

assemblage (relative abundance of major diatom taxa) in the subsamples, the counted number of diatom valves was usually >200 valves for each subsample.

It is important to emphasize the distinction between the diatom analysis of the smear slides and of the BSEI of polished thin sections (PTS). The smear slide analysis using conventional methods including optical microscopy represents a traditional method, but the smear slides involve taking a sediment sample that includes several laminae and generally several mm. On the other hand, the BSEI of PTS analysis involves resolving diatom composition on a scale of 1/10th mm or less. In this way, the BSEI often resolve individual seasonal-scale flux events dominated by a single or a few taxa, whereas the smear slides homogenise may flux events, and so act to "average" the composition over a significant time interval that is likely to encompass several years.

The shortcoming of the BSEI method is that the diatom valves are generally seen in cross section which can make the identification of individual taxa difficult. To aid BSEI identification (Fig. 3), subsamples of laminae are taken for topographic SEM analysis (Fig. 4). Furthermore, because some taxa are similar in cross section, they cannot be distinguished in BSEI, hence the "discoidal" group described above that pools three taxa.

3.2. Rare Earth Element (REE) analysis

The dry bulk sediments (0.22–45.09 mg) from the subsamples were dissolved in a 3:1 mixture of ultrapure concentrated HNO_3 and HF (TAMAPURE-AA-100 from Tama Chemicals, Ltd., Tokyo) for >24 h on a hotplate (130–140 °C). Rare earth elements (REEs) were separated by a conventional cation-exchange resin column (Mitsubishi diaion CK08P, 75–150 μm) using 1.7 M HCl and 6 M HCL as the eluent (Yamamoto et al., 2005; Horikawa et al., 2015). The sample solution was then redissolved with an In-spiked dilute ultrapure nitric acid solution (2% HNO_3), and the REE concentration was determined with a Thermo Scientific ELEMENT 2 sector field inductively coupled plasma mass spectrometer (SF-ICP-MS) at the University of Toyama. The relative standard deviation ($n = 3$) of the REE concentration measurements for the reference rock material (BCR2) was <3%, and the difference from the reference value was <5% for all REEs except for La (14%). The REE concentrations were not corrected.

Core-top REE composition and downcore neodymium (Nd) isotopic compositions in the Bering Sea vary in response to the changes in relative contributions of sediment from the Aleutian Arc or Alaska sources, and thus REE and Nd isotopic compositions have been used to reconstruct paleoceanographic conditions (Asahara et al., 2012; Horikawa et al., 2015). According to the core-top REE data by Asahara et al. (2012), the Europium anomaly (Eu/Eu*) can be used for identification of sources of clastic detrital sediments in the Bering Sea. A high Europium anomaly (Eu/Eu*) of ~1.0 is observed near the Aleutian arc, while lower ratios of 0.85–0.88 are measured in the Chukchi Sea and off the Mackenzie Delta in the Beaufort Sea. Intermediate Eu/Eu* ratios of 0.90–0.93 and 0.93–0.98 are observed in northern and southern areas of the Eastern Bering Sea shelf, respectively (Asahara et al., 2012). In addition, this study also examined differences in REE patterns based on the ratio of light REEs to high REEs (LREE/HREE), as Asahara et al. (2012) did for La/Lu in their evaluation of the origin of the lithogenic matter in the sediments. The calculated LREE/HREE based on the dataset of Asahara et al. (2012) shows that the LREE/HREE of the northeastern shelf is ~6.9 whereas that of the southeastern shelf is ~3.5.

3.3. Cyclicity analysis

The cyclicity in the lamina thickness and diatom composition in PTS was checked using the statistics software "R" and the package for the continuous wavelet analysis "WaveletComp 1.1" (Roesch and

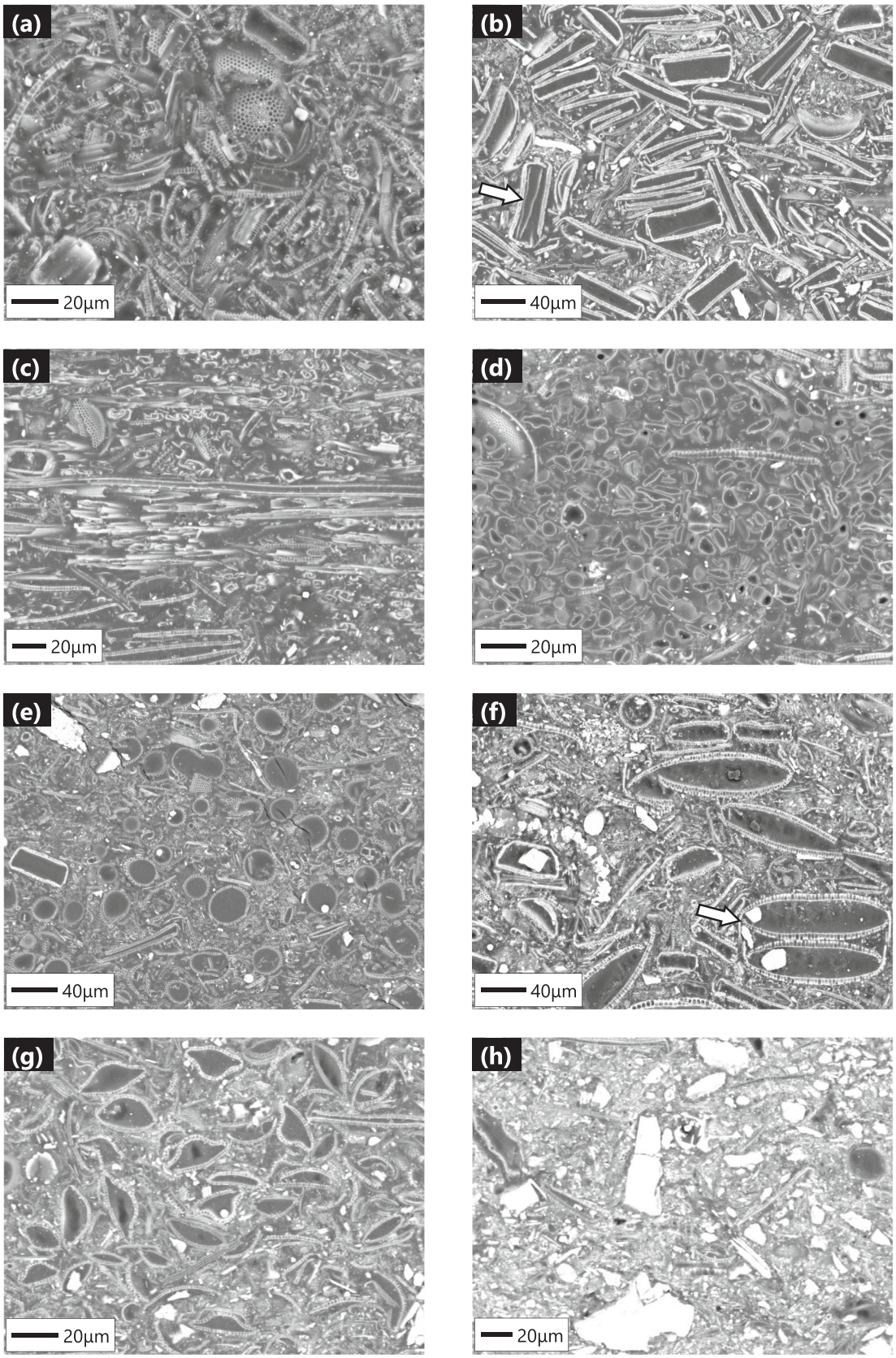

Fig. 3. Back-scattered SEM images on thin sections. Scale bars = 20 μm except for (b), (e), and (f) showing 40 μm. The dominance of (a) *Neodenticula seminae* and *Shionodiscus*, (b) *Actinocyclus*, (c) *Thalassiothrix*, (d) *Chaetoceros* resting spores, (e) *Eupyxidicula*, (f) *Coscinodiscus*, (g) *Thalassiosira antarctica* resting spores and (h) lithogenic material. The arrow in (b) and (f) shows a cross-section of diatom frustule in cell division.

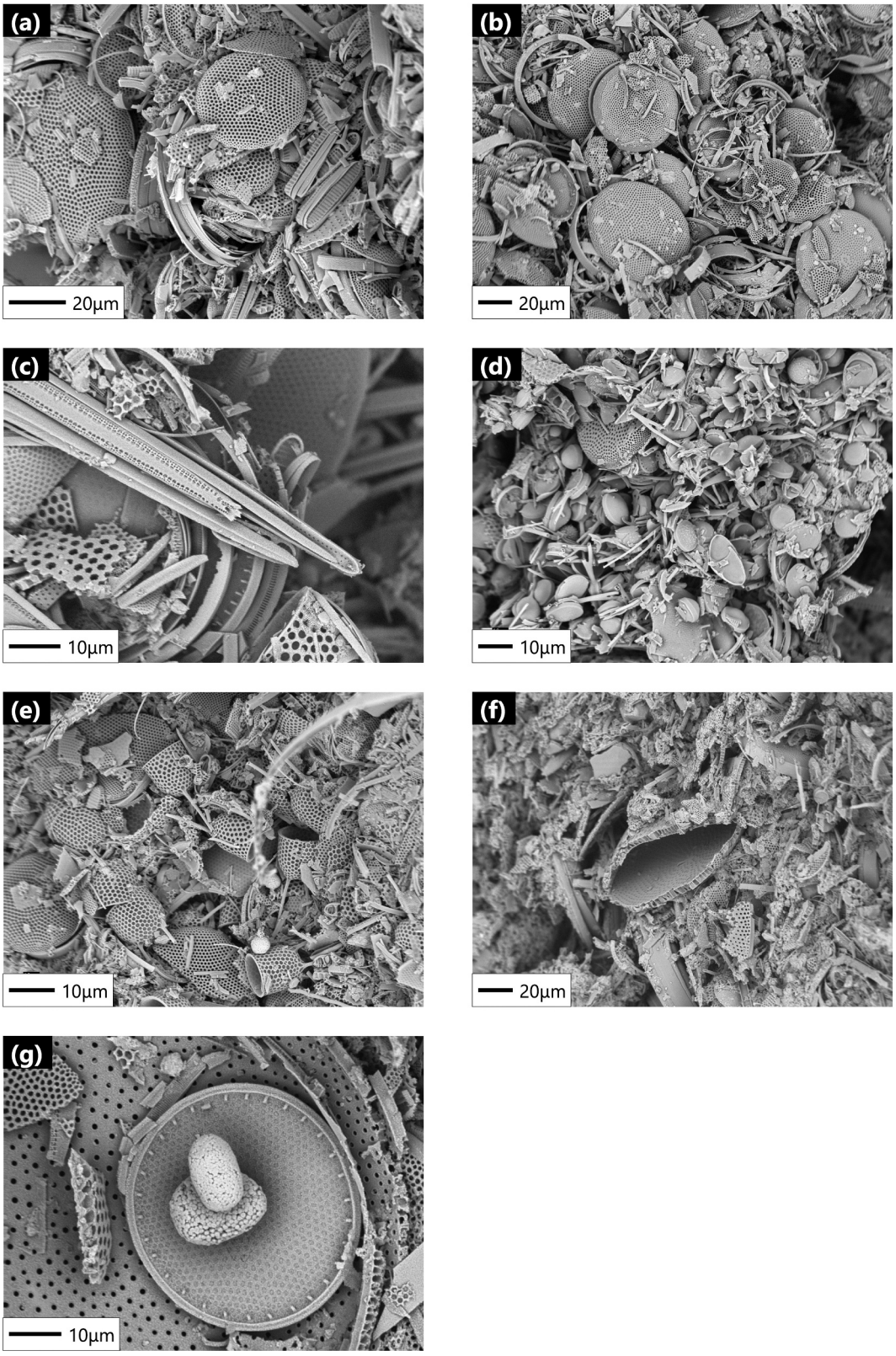

Fig. 4. Back-scattered topographic SEM images on the surface of the crack of laminated subsamples. Scale bars = 10 μm except for (f) showing 20 μm. (a) *Neodenticula seminae* and *Shionodiscus*, (b) *Actinocyclus* and *Shionodiscus*, (c) *Thalassiothrix*, (d) *Chaetoceros* resting spores, (e) *Eupyxidicula*, (f) cross-section of *Coscinodiscus*, and (g) framboidal pyrites on diatom valve of *Shionodiscus*.

Table 1
Diatom taxa/ categories identified in cross section in BSEI of polished thin sections (PTS) of resin-embedded sediment.

Diatom taxa/ categories in BSEI cross section	comment
Neodenticula	
Discoidal (taxa that could not be easily distinguished from each other in cross section)	Includes the genera *Actinocyclus* spp., *Shionodiscus* spp. and *Thalassiosira* spp.
Thalassiothrix	
Setae (spines)	Mainly the setae of *Chaetoceros* spp.
Chaetoceros spp. resting spores	
Eupyxidicula	
Coscinodiscus	
Odontella	
Asteromphalus	
Thalassiosira antarctica resting spores	
Proboscia and *Rhizosolenia* spp.	Rhizosolenid diatoms
Others	

Schmidbauer, 2018). The dataset on diatom PTS was detrended with the "loess.span" setting ($\alpha = 0.75$) in the WaveletComp. The *p*-value was calculated with a MA(1) model. In cases where the organic lamina had been divided into some sub-layers, these were combined to form one lamina before the cyclicity analysis to keep the even time interval as annual data which is a couplet of organic and lithogenic layers (the varve).

4. Results

4.1. Structure and thickness of laminated sediments

Detailed BSEI of polished thin sections of resin-embedded sediment revealed a regular alternation between laminae comprised of pure diatom ooze, with laminae rich in lithogenic material (Fig. 5). Although many of the studied laminations are parallel, some laminations are unclear by the slight bioturbation including that of benthic foraminifers. There was no evidence for discontinuities or micro-unconformities in the sequences. There was also no evidence of bottom current activity, such as erosive contacts or current winnowing effects. Overall, the detailed BSEI fabric analysis appears to indicate the presence of uninterrupted sequential flux events.

The thickness of studied lamina facies is approximately 29.2 and 12.0 cm for Sections 10H and 14H, respectively. The studied sample for Section 10H was divided into two parts by core cutting between Sections 10H-1 and 10H-2 (Fig. 6a, b). The disturbed core-cutting part between the sections is not recovered by another hole because other drilling holes at Site U1340 did not reach the depths of the studied age interval (Takahashi et al., 2011). The lamination for Section 14H was interrupted by 27 mm thickness of homogenous sediment (Fig. 6e, f).

The number of identified laminations is 514 and 230 for Sections 10H and 14H, respectively. The thickness of lamination varied from 0.16 to 1.69 mm with a mean thickness of 0.57 ± 0.27 mm (1SD) and the median of 0.51 mm for Section 10H, and from 0.12 to 2.33 mm with the mean of 0.52 ± 0.30 mm (1SD) and the median of 0.44 mm for Section 14H (Fig. 6b, f). The mean thickness of the diatom laminae (0.61 ± 0.30 mm) for Section 10H is slightly larger than that of the lithogenic-rich layer (0.54 ± 0.29 mm, $p < 0.05$). The mean thickness of the diatom and lithogenic-rich laminae for Section 14H is almost the same (diatom layer: 0.52 ± 0.34 mm, lithogenic layer: 0.53 ± 0.26 mm). Planktic foraminifer shells were abundant in a few biogenic laminations. Temporal abundant settlement of planktic foraminifera shells and volcanic ash might contribute to some of the unusual thick laminations.

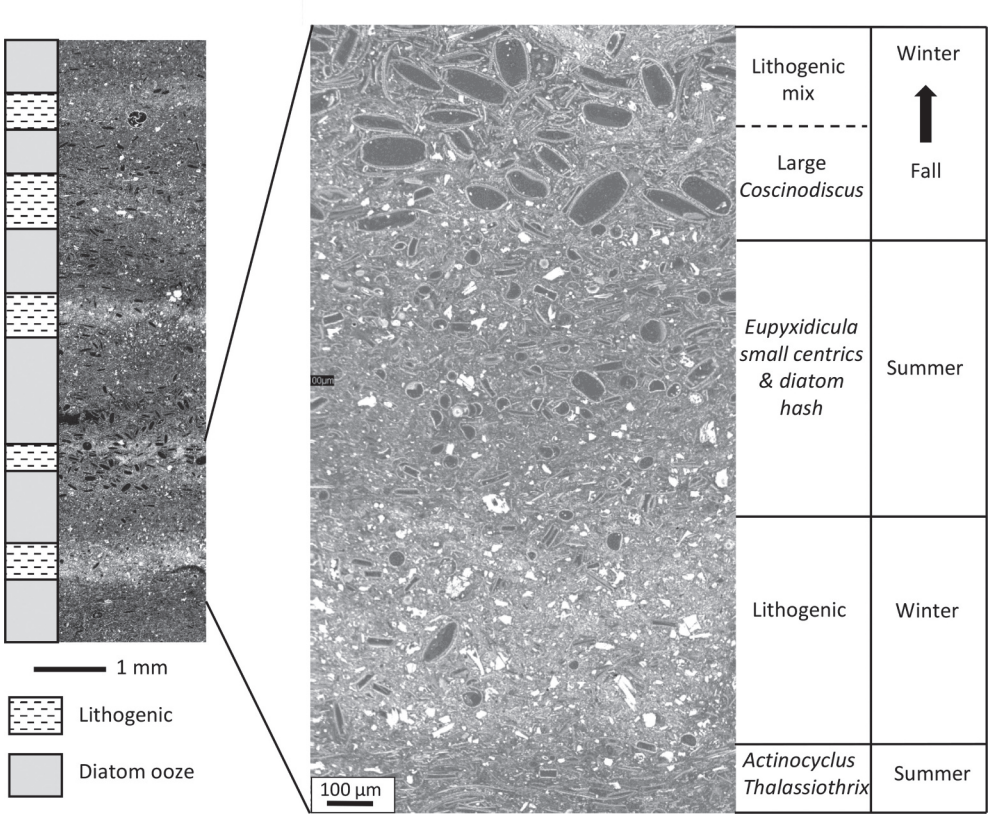

Fig. 5. Detail of changes in flux through an annual cycle. The left panel shows alternation of lithogenic and diatom laminae. The right panel shows changing diatom flux within one annual cycle.

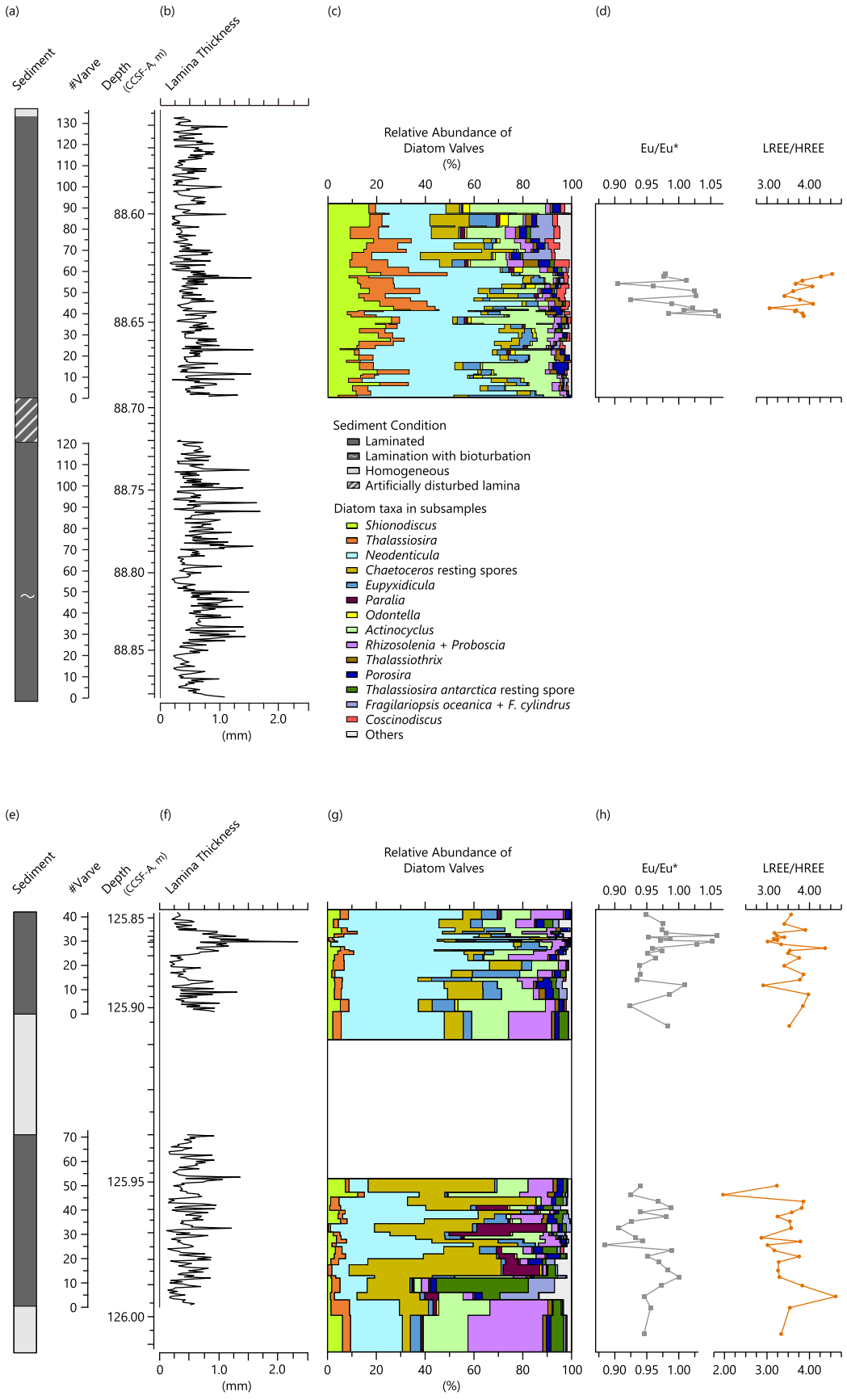

Fig. 6. Sediment condition of studies samples, time-series of lamina thickness, diatom assemblage of smear slide subsamples, the europium anomaly (Eu/Eu*), and the HREE/LREE ratio. Eu anomaly is defined as Eu/Eu* = log(Eun)/{log(Smn) + log(Gdn)}/2. LREE and HREE are (Lan + Prn + Ndn) and (Hon + Ybn + Lun),

respectively. Values denoted as n are normalized by CI-chondrite (Anders and Grevesse, 1989). The upper and lower panels show the results for Sections U1340A-10H and 14H, respectively.

4.2. Diatom Ooze laminae

The ooze laminae most commonly comprise concentrations of intact diatoms of a single or a few dominant species with other more minor species in subordinate amounts (Figs. 3, 4). In some instances, it is evident that diatom cells were undergoing active division (Figs. 3b, f). Some of the diatom ooze laminae are composite with sub-laminae of differing species (Fig. 5). Up to three sub-laminae of different diatom flora were recorded. In such cases, the lower sub-lamina commonly include resting spores, while the upper laminae may contain large *Coscinodiscus*. In some laminae there is a variable, but generally minor component of fragmented diatom material. There is also commonly a very minor component of terrigenous material, mainly very fine silt and clay.

4.3. Lithogenic laminae

The lithogenic laminae are poorly sorted and comprise mainly clay and fine to very fine silt (<16 μm) with minor medium silt (<32 μm). This is mixed with variable amounts of diatomaceous material which is often fragmented. Larger grains of coarse silt up to, but never exceeding fine sand (<250 μm) occur more rarely and are commonly present in the lithogenic laminae or may also occur as isolated grains within the diatomaceous laminae. In some cases (Fig. 7), the coarser silt or sand grains occur along the same level, evidently recording synchronous deposition. These layers of coarser grains commonly occur associated with or just below the main lithogenic lamina in the sequences. The layer of coarse grains shown in Fig. 7 separate biogenic laminae of different diatom composition.

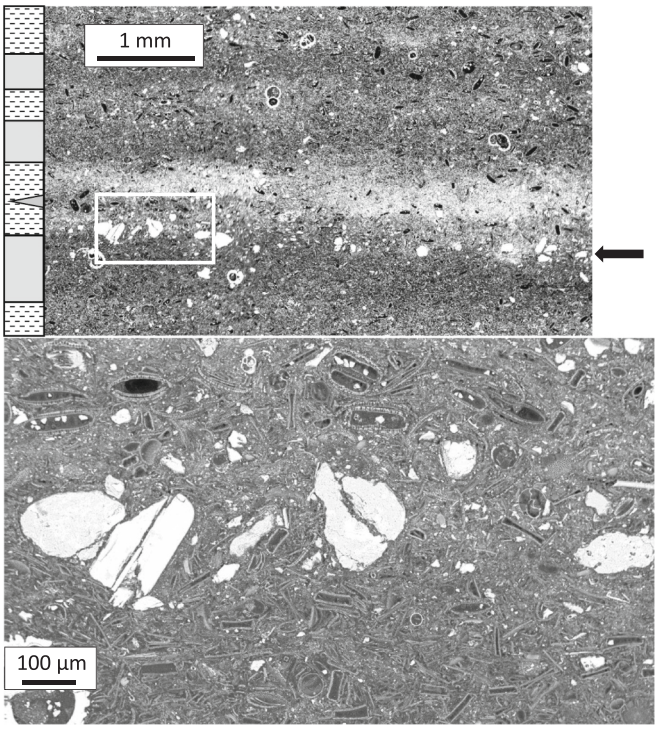

Fig. 7. General view and detail of a train of isolated fine sand and silt grains. The grain with prominent cleavage is a K-feldspar, the others are mainly altered volcanic grains including calcic plagioclase and pyroxene with chlorite and clay. Note the difference in diatom flora below and above the grains.

4.4. Diatom composition and REE

4.4.1. Marine Isotope Stage 13 (Section 10H-1 and -2)

According to diatom BSEI PTS analysis (because no smear slide subsamples are available for the Section 10H-2), major diatom taxa in the initial period of laminated sedimentation were *Chaetoceros* and *Thalassiothrix* (Fig. 8c). The temporal increase of *Neodenticula seminae* higher than 20% started after ~28 varve numbers from the initial lamination of this section. The "discoidal taxa" in diatom BSEI PTS analysis are *Thalassiosira* (except for *T. antarctica* resting spore), *Shionodiscus*, in addition to *Actinocyclus* (Figs. 6c, 8c). In the smear slide diatom assemblage (Fig. 6), the relative abundance of *Fragilaripsis cylindrus* + *F. oceanica* increased in the upper part of the studied interval for Section 10H-2 (Fig. 6c). *Rhizosolenia, Proboscia* and *Chaetoceros* resting spores in the diatom assemblage of smear slides were minor compared to their relative abundances in Section 14H-1 as shown below (Fig. 6c, g), except in the uppermost part.

The REE ratios were conducted for a limited number of subsamples (Figs. 6, 9). The ratios of Eu/Eu* (0.88–1.07) and LREE/HREE (3.07–4.53) suggest that much of the lithogenic matter had been supplied from both the Aleutian Islands and the southern Bering Sea shelf.

4.4.2. Marine Isotope Stage 19 (Section 14H-1)

The diatom assemblage in smear slide subsamples of the earlier part for Section 14H was characterized by the common occurrence of the *Rhizosolenia* + *Proboscia* group in addition to temporal increases of *Chaetoceros* resting spores, *Paralia sulcata,* and *Thalassiosira antarctica* resting spore (Fig. 6g). *Neodenticula seminae* was partially dominant for the lower part of Section 14H-1 subsamples, and then their dominance was continuously observed in the upper part of Section 14H-1 (Fig. 6g). The relative abundances of *Thalassiosira* and *Shionodiscus* in the diatom assemblage of smear slides from Section 14H-1 were lower than those in Section 10H-1 (Figs. 6c, g). In the smear slide subsample near the initial lamination (corresponding to varve #2.5–5), oceanic diatom *N. seminae* was a relatively minor component in the diatom assemblage whereas cold-water taxa such as *Fragilariopsis oceanica, F. cylindrus,* and *Chaetoceros* spp. resting spores were relatively abundant. *Thalassiosira antarctica* resting spore was common around the initial laminated period (~ Varve #10).

Diatom BSEI PTS counts showed that the dominant species was variable, commonly changing on time scales of a few years to decades. The dominant taxa in BSEI PTS counts were the discoidal group (*Actinocyclus* spp., *Shionodiscus* spp., *Thalassiosira* spp. except for *T. antarctica* spore) with *Neodenticula seminae*, *Thalassiothrix* group, and setae of *Chaetoceros* spp. (Fig. 8f). *Thalassiosira antarctica* resting spore was temporally abundant at the lower part, which was also observed in the subsample smear slide (Fig. 6g). *Paralia sulcata* was temporally dominant in BSEI at varve numbers of ~14–15 and ~ 31 (Fig. 8f).

The REE data for this MIS19 interval showed that Eu/Eu* ranged from 0.85 to 1.06 (Fig. 6h, 9). The mean of Eu/Eu* ratio in the lower laminated part (0.94 ± 0.04) was slightly lower than that in the upper part (0.98 ± 0.04). The LREE/HREE ranged from 1.97 to 4.61 (Fig. 6h, 9). This is again consistent with supply from both the Aleutian Islands and the southern Bering Sea Shelf.

4.5. Cyclicity

There was no clear periodicity in time series fluctuation of lamina thickness throughout each laminated section. However, detrended accumulated thickness showed a period of ~19 years ($p < 0.01$) for the lower part of 14H-1 (Fig. 10c-e). The accumulated thickness for other parts showed longer decadal variations although the statistical

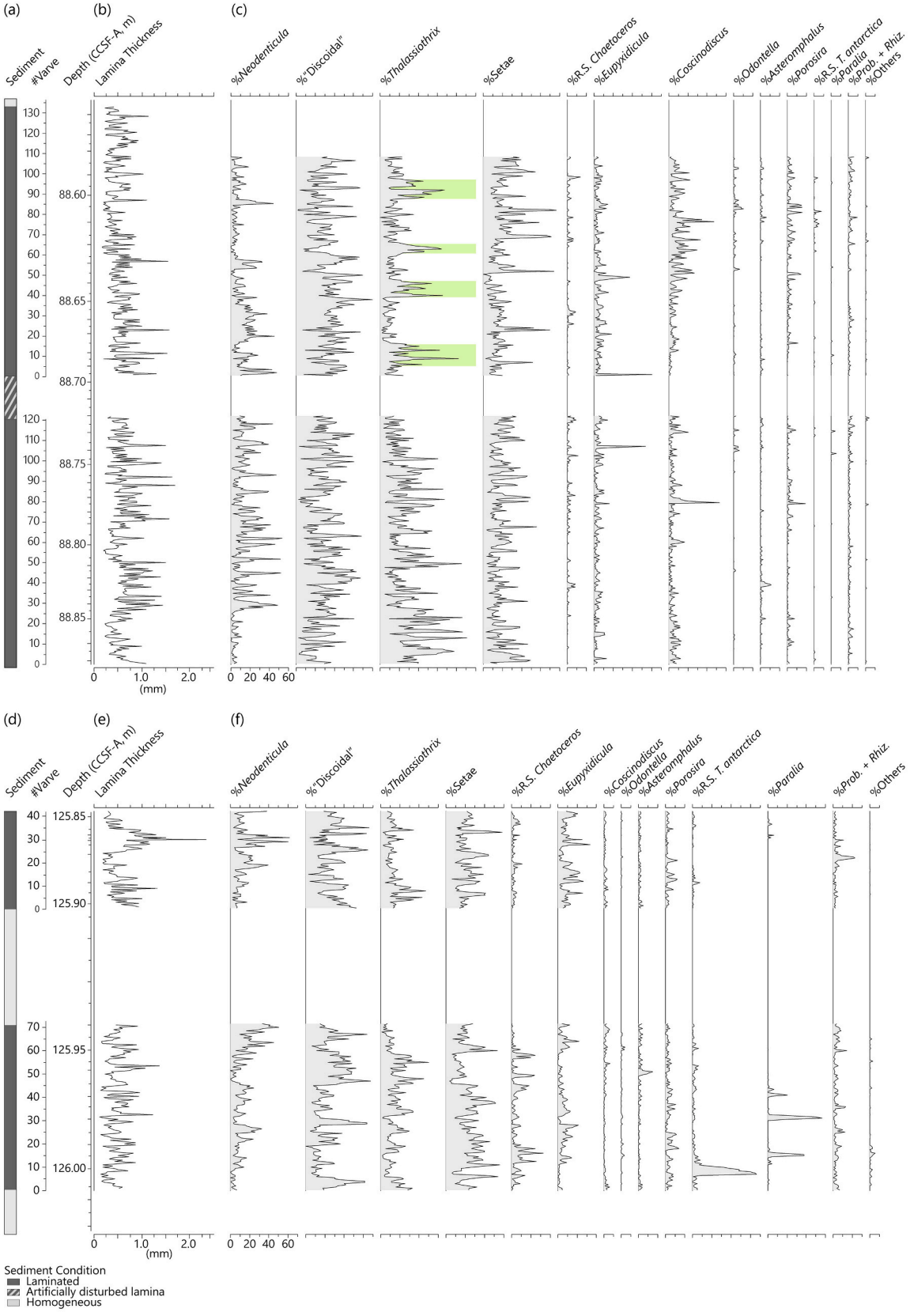

Fig. 8. Time-series of the relative abundance of diatoms from BSEI PTS analysis encountered in each lamina of thin section. The upper and lower panels show the results of Sections U1340A-10H and 14H, respectively. In the upper panel (c), the ~ bi-decadal-scale recurrence of peaks in *Thalassiothrix* abundance are indicated by the shading.

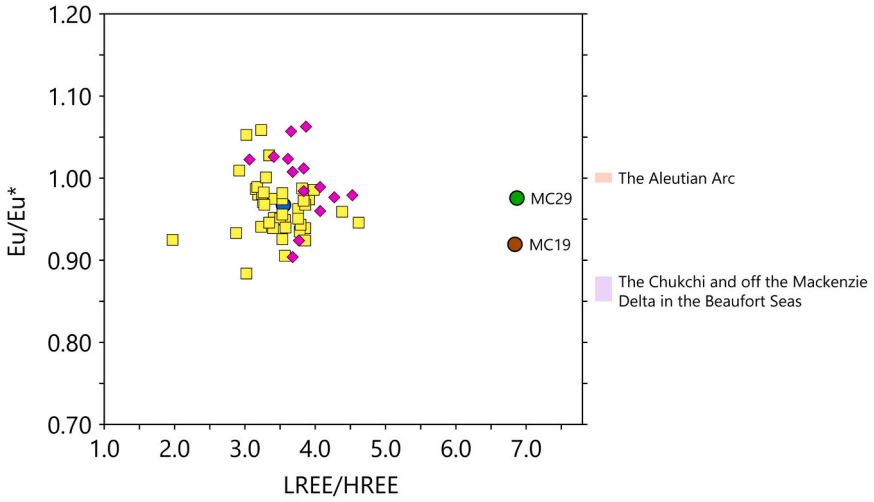

Fig. 9. The ratios of LREE (La—Nd)/HREE (Ho—Lu) and Eu/Eu*, plotted as yellow rectangular and magenta rhombic symbols for Sections U1340A-10H and 14H, respectively. The circular symbols in brown, green, and blue correspond to the cored positions MC33, 29, and 19 of Asahara et al. (2012), respectively (Fig. 1). (For interpretation of the references to colour in this figure legend, the reader is referred to the web version of this article.)

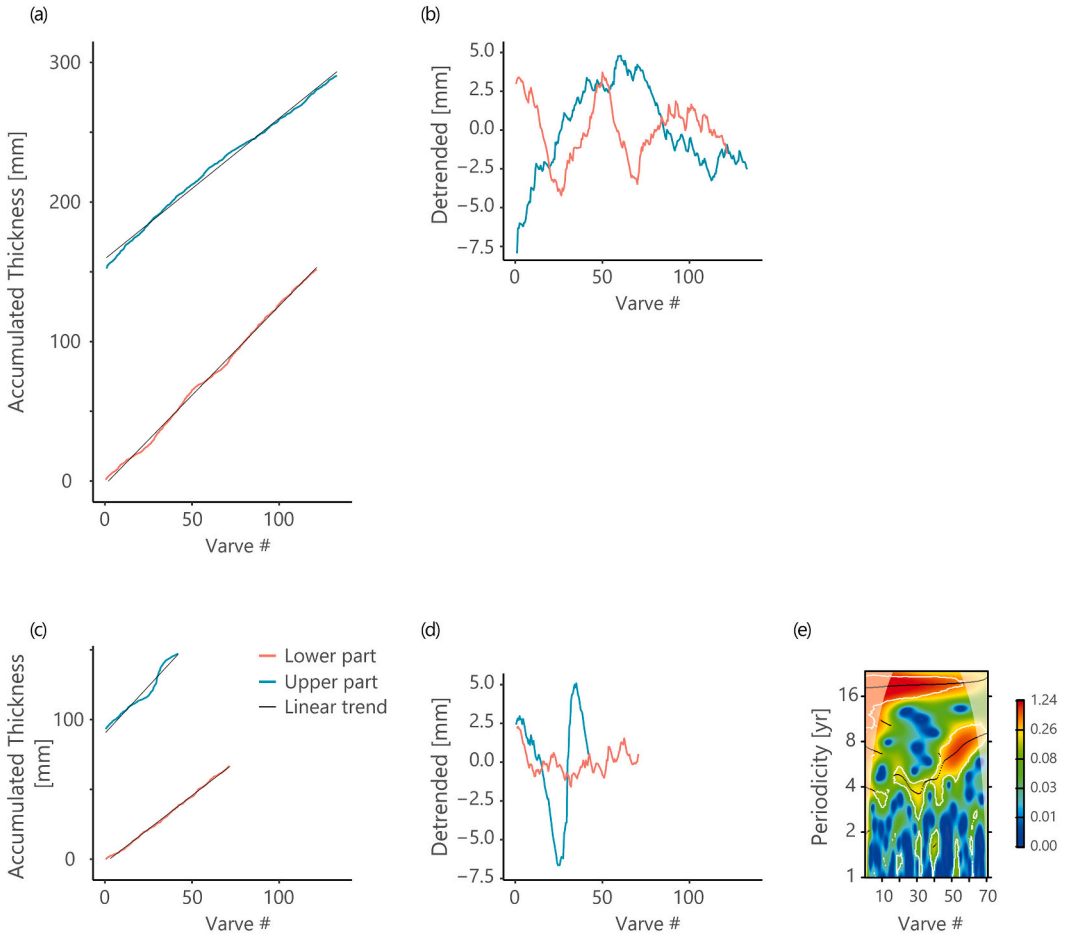

Fig. 10. The accumulation rate of varve thickness shows a decadal change. (a) the relationship between varve numbers and accumulated lamina thickness, and (b) the detrended change in accumulation rate of lamina thickness for ~528 ka. (c) and (d) is the same as (a) and (b), but for ~782 ka. (e) The results of wavelet time-series analysis for the lower part of ~782 ka. The white contour represents a significant level of $p = 0.05$. The black dotted line shows the ridge position of the power spectrum.

significance on the periodicity was not obtained due to the short duration of the laminated section (Fig. 10).

The PTS diatom assemblage also showed distinct periodicities (Fig. 11). In Section 10H-1 a sustained periodicity of ~26.5 years for *Thalassiothrix* was clear (Fig. 11a). A bi-decadal periodicity in this section for the recurrence of *Thalassiothrix* abundance is also evident from

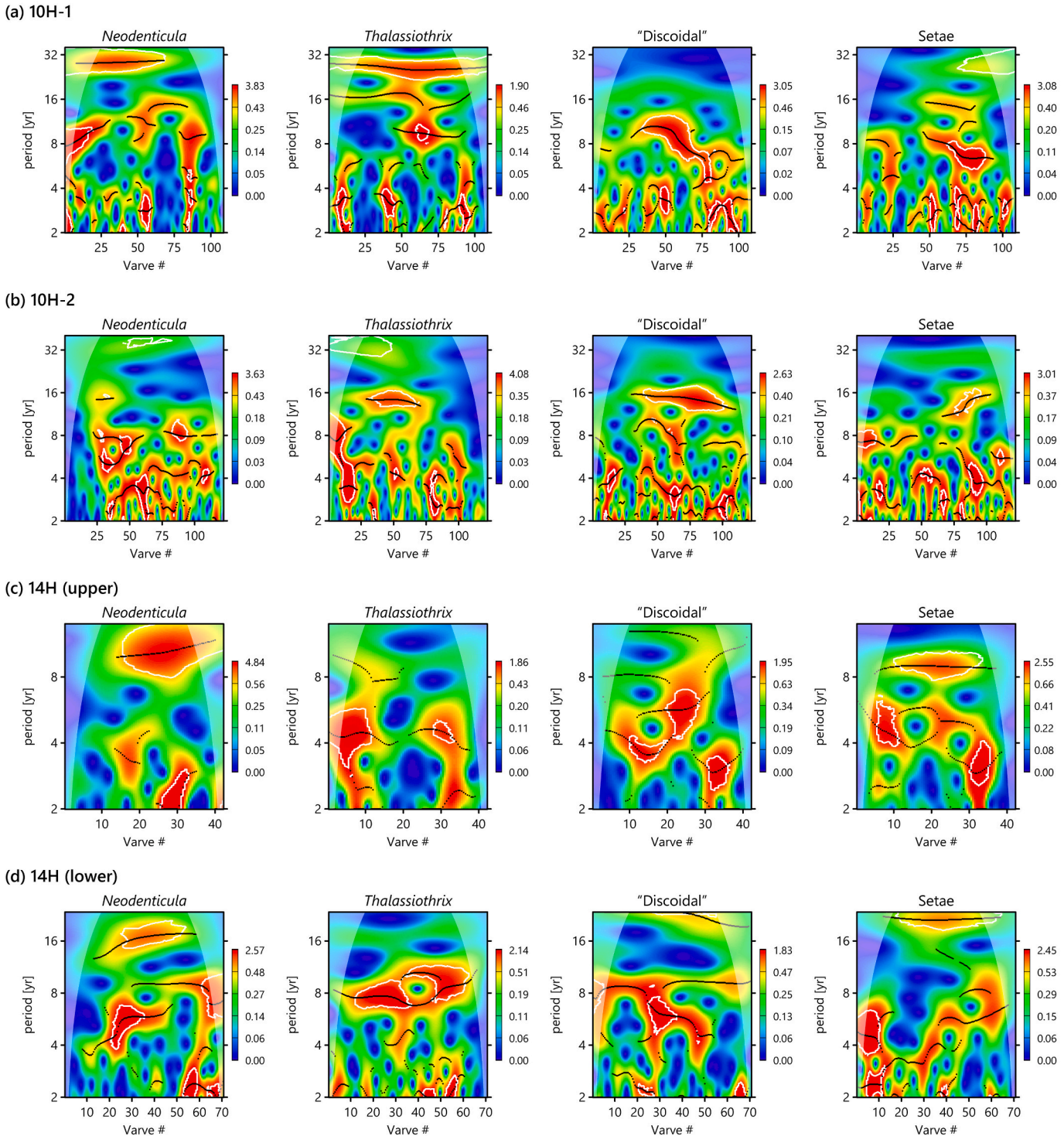

Fig. 11. Continuous wavelet analysis on the major diatom taxa of PTS diatom composition. The white line contour represents a significant level of $p = 0.05$. The black dotted line represents a ridge position of spectral power.

the diatom BSEI PTS count plots (Fig. 8c). *Neodenticula* also showed a periodicity of ~30 years. *Neodenticula* and setae in Section 14H-1, also partly showed decadal periodicity (Fig. 11). In all records there are non-stationary (more discontinuous) periodicities in the 4–8 year and quasi-biennial bands.

5. Discussion

5.1. Annual/ varve interpretation for the diatom–lithogenic couplets

5.1.1. Diatom Laminae

The diatom laminae evidently represent flux from active surface blooms or concentrations. The typical dominance of one or a few species in individual laminae emphasize the key taxa involved in driving the bloom events. The *Chaetoceros* spp. resting spores represent flux from

early season spring blooms, which might be different from the modern situation showing a seasonal flux maximum in late spring - early summer in the Aleutian Basin as a possible reflection of nutrient-rich water advection from the Aleutian Island passes (Onodera and Takahashi, 2009). The main spring and summer blooms comprise, often near monospecific, concentrations of vegetative cells of *Shionodiscus trifultus*, *Thalassiosira* spp., *Actinocyclus curvulatus*, and *Neodenticula seminae*. The evidence of active division in some of the cells present, including those of *S. trifultus* and *Coscinodiscus* spp. (Figs. 3b, f) highlights the healthy bloom dynamics. Also present in bloom concentrations in some laminae are *Rhizosolenia* spp., *Proboscia* spp., *Thalassiothrix longissima*, and *Eupyxidicula* spp. (Fig. 5), and these species likely indicate stronger summer stratification (Kemp et al., 2000). The presence of abundant intact cells evidences minimum involvement of zooplankton so that it is likely that the laminae represent "self-sedimentation" events that would have occurred towards the end of spring/ summer bloom events when nutrients were running out, especially so, in the case of laminae dominated by resting spores (Figs. 3d, g). The composite laminae that include layers or sub-laminae of different diatom taxa likely record a seasonal succession of diatom production (Fig. 5). The common occurrence of large *Coscinodiscus* spp. in the upper (later) flux layer likely records the breakdown of stratification with the advent of winter storms in a "fall dump" flux (Kemp et al., 2000).

5.1.2. Lithogenic laminae

The clay and fine silt component are likely the product of hemipelagic settling and this would be more active during the period of winter storms and enhanced river runoff (Mesquita et al., 2010). However this would be unlikely to contribute grains larger than around 40 μm (Hebbeln, 2000). It is therefore necessary to provide an explanation for the presence of sand up to, but not exceeding fine sand grade (250 μm).

The likely mechanism for the 250 μm cut-off is the formation of turbid ice by suspension freezing and subsequent sediment entrainment (Smedsrud, 2001). This involves the formation of frazil ice crystals in turbulent supercooled water that is typically generated in autumn or early winter storms (Kempema et al., 1989; Smedsrud, 2001). The newly formed frazil ice crystals scavenge sedimentary particles suspended by the storm waves and rise to the surface to form a sediment-laden granular ice that may then freeze further to give turbid ice (Fig. 12). Experiments have shown that no grains larger than fine sand (250 μm) can be suspended by frazil ice with larger grain sizes settling with the ice to the sea bed (Smedsrud, 2001). This same 250-μm cut-off in our lithogenic material suggests the same mechanism. Significantly, newly formed slush ice is highly mobile and is capable of rafting several hundred km from source in the modern Arctic (Sherwood, 2000; Meese et al., 1997), so that such material would easily have reached the Bowers Ridge site. The presence of very labile grains including altered igneous material such as calcic plagioclase and pyroxenes with chlorite and clay (Fig. 7) further indicates minimal transport and is also consistent with a rafting origin, likely from the Aleutian arc. Lithogenic material of similar grain size, ascribed to the same origin has been described in diatom ooze of Cretaceous age from the Alpha Ridge of the Arctic Ocean (Davis et al., 2009).

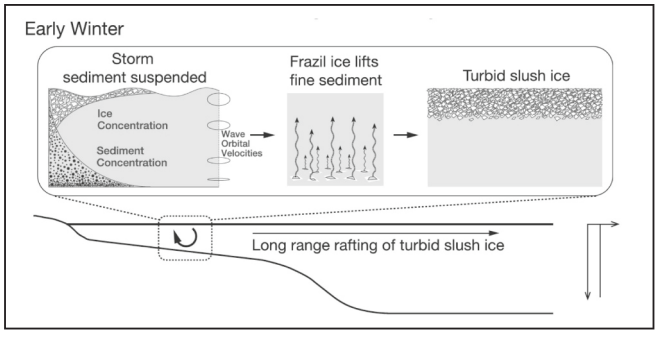

Fig. 12. Cartoon showing the formation of turbid ice adapted from Smedsrud (2003).

Interestingly, granulometric studies of recent sediments from the Bowers Ridge and from the Shirshov Ridge, define 3 lithogenic sediment particle size end members. Two identified end member components are primarily clay and silt and are ascribed to hemipelagic sedimentation sourced primarily from riverine input (Murdmaa et al., 2019; Wang et al., 2016, 2021). Both these groups define a third end member in the coarse silt to fine sand range. Murdmaa et al. (2019) ascribe this fraction to rafting of fast ice, while Wang et al. (2016, 2021) adopt winnowing by bottom currents. Neither of these mechanisms can account for our SEM sediment fabric observations, since fast ice would contain abundant material coarser than fine sand which is not present in our intervals. Moreover, winnowing would result in sorting of the particles, whereas the coarse silt and fine sand we observe is clearly unsorted. It may be that the coarse silt/ fine sand fraction in these recent Bering Sea sediments are, in fact, due to rafting of turbid ice.

5.1.3. Summary of the annual flux cycle

We may now combine the interpretations of the diatom and lithogenic laminae to reconstruct the annual flux cycle in the two intervals (Fig. 13). Early season blooms are evidenced by the occurrence of laminae dominated by the resting spores of *Chaetoceros* spp. and more rarely of *Thalassiosira antarctica* that generally occur immediately above

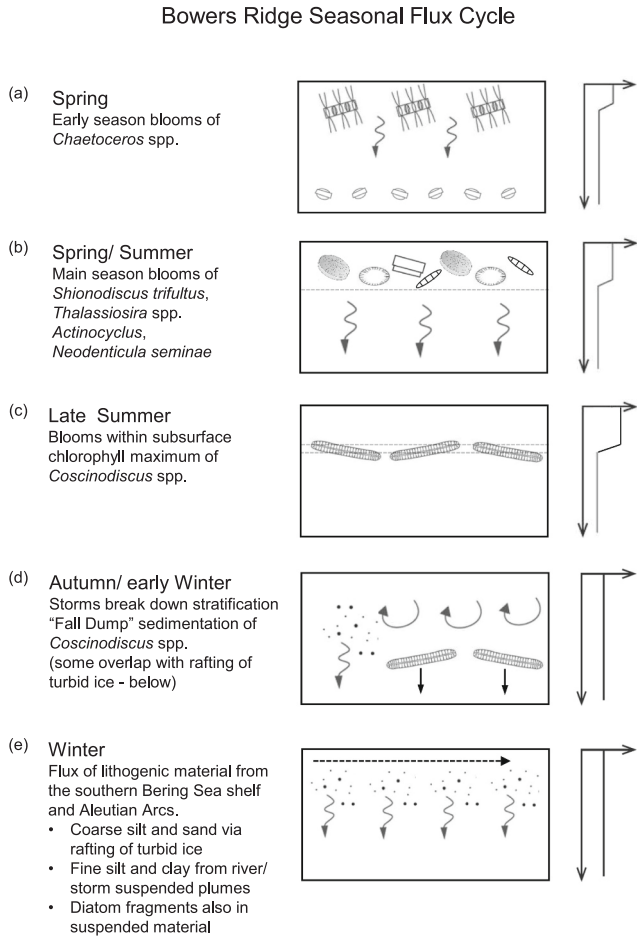

Fig. 13. The reconstructed seasonal cycle showing the succession of distinct flux episodes that combine to give the diatom–lithogenic lamina couplets. The right-hand panels are schematic plots of temperature with depth indicating the seasonal development and breakdown of water column stratification.

the winter lithogenic lamina (Fig. 3d, g, 4d). Where abundant (Fig. 6; Fig. 8f), the presence of *T. antarctica*, likely indicates enhanced meltwater influence during the spring bloom (Krawczyk et al., 2012). Blooms of *Chaetoceros* spp. are typical of spring productivity in high northern latitudes, although at Station AB in the modern Aleutian Basin (Fig. 1) they tend to occur later in the summer (Onodera and Takahashi (2009). The diatom laminae containing concentrations of vegetative cells of *Shionodiscus trifultus*, *Thalassiosira* spp., *Actinocyclus curvulatus*, and *Neodenticula seminae*, represent flux from the main spring-summer bloom episodes and are typical of modern summer blooms in the Bering Sea and North Pacific (Takahashi et al., 2000, 2002; Onodera and Takahashi, 2009). The presence of *N. seminae*, indicates influx of seed populations from the North Pacific Alaskan Stream (see discussion in 6.2.1, below). The common occurrence of dividing cells of these taxa (Fig. 3b, f) suggests sedimentation of actively blooming populations, possibly in response to disruption of stratification by occasional summer storms. Concentrations of *Coscinodiscus* spp. generally occur near in the uppermost part of the diatom laminae (Fig. 5) likely representing flux driven by autumn or early winter storm events disrupting summer stratification in "Fall Dump" events (Kemp et al., 2000). In some cases, *Coscinodiscus* spp. also occur associated with the lower parts of the lithogenic laminae (Figs. 5, 6), likely signifying early winter flux. The coarsest component of the lithogenic material (fine and very fine sand) was contributed by rafting of turbid ice generated by early winter storms (Fig. 13d). The finer component of the lithogenic layers includes sediment suspended by winter storms and input by rivers that formed hemipelagic settling plumes distributing silt and clay material throughout the Bering Sea.

The overall particle settling flux for the studied intervals was significantly higher than that in modern conditions. Annual daily mean on total settling particle flux for the both periods is estimated as at least ~1 g m^{-2} day^{-1} based on the varve thickness and sediment dry bulk density as 0.37 g cm^{-3} obtained from diatomaceous laminated sediment at Site U1342 on the northern top of the Bowers Ridge (Takahashi et al., 2011) (Fig. 14). Compared to the modern settling particle flux monitored at Station AB (Fig. 1), the estimated settling flux of total mass flux (TMF) for the studied intervals was ~5 times greater. This further confirms the greatly enhanced productivity during these laminated intervals and fits the models that associate lamina preservation with reduced bottom water oxygen due to enhanced productivity and flux during these episodes (Knudson et al., 2021; Praetorius et al., 2015). The coefficient of variance for the estimated TMF (38.6 and 62.6 for 10H and 14H, respectively) was larger than that of modern TMF (28.2). This suggests larger interannual variability in the past TMF, probably as a reflection of more changeable hydrographic conditions in the upper water column compared to the modern situation.

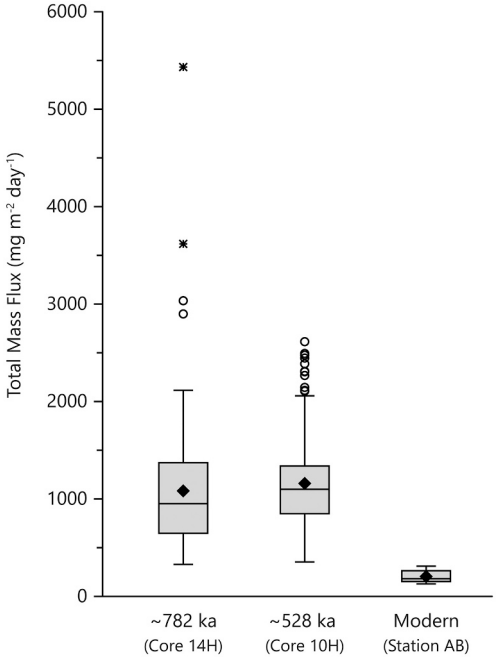

Fig. 14. Box plots on annual mean of daily total mass flux for comparison of this study and the modern data obtained at Station AB for 1991–1998 and 2003 (Fig. 1, Takahashi et al., 2000, 2002, 2012a,b). Whiskers show the largest and the smallest data in an inner fence of the box plots. The data outside the inner fence are shown as the circular symbol and the star symbol for the data over the outer fences. The rhombic symbol represents the mean value.

5.1.4. Lamination and climatic cyclicity

Some cyclicities estimated in the lamina thickness and BSEI PTS diatom composition may reflect variation in climate and ocean dynamics. Sub-decadal monitoring of sinking diatom flux at Station AB shows the possible relationship between the diatom sinking flux and mixing layer depth in annual mean data (Onodera and Takahashi, 2009). In the modern ocean, six groups of periodicities have been found in the range from about 3 to about 32-years (Seip and Grøn, 2019). The estimated cyclicity of ~19 years in the lamina thickness might reflect ocean dynamics. Lunar tidal mixing with 18.6 years periodicity is important for long-term sea surface temperature change in the modern North Pacific (Osafune et al., 2014).

In the upper part of the MIS 13/ 10H sequence there is a strong and persistent 26.5 year periodicity for *Thalassiothrix*, and a bi-decadal occurrence of *Thalassiothrix* maxima is also evident in this section from the diatom BSEI PTS abundance plots (Fig. 8c). This suggests some bi-decadal variation in the degree of stratification and/or frontal zone activity. In the same interval, *Neodenticula* also shows there is also a ~30 year periodicity. This suggests a periodic increase in penetration of Alaskan Stream waters (see 6.2.1, below). A 20–30 year period is typical of the Pacific Decadal Oscillation (PDO) (Gedalof et al., 2002). The positive phase of the PDO strengthens the Alaskan Stream (Yang et al., 2020) and this would likely increase flow through the Aleutian Islands bringing increased *Neodenticula*. The strengthened Alaskan Stream also brings enhanced northward heat transport driving surface warming and density decrease in the Bering Sea (Yang et al., 2020), and the subsequent increase in stratification would favour *Thalassiothrix*.

The non-stationary quasibiennial and 4–8 year periodicities seen in the diatom BSEI PTS likely reflect ENSO influence. A study of thickness variability of laminae from X-ray images in sediments of Bølling Allerød age from the Bering northern continental slope gave a periodicity of 11 years ascribed to solar influence on ice melt and productivity (Katsuki et al., 2014), but there was no corresponding signal in our sequences.

5.2. Paleoclimatic and hydrographic reconstruction from diatom assemblages

5.2.1. Significance of Neodenticula seminae as an environmental indicator

In the modern Aleutian Basin, the dominant diatom species in settling particles at Station AB (Fig. 1) is usually *Neodenticula seminae*, with occasional and short-lived dominance of *Chaetoceros* resting spores (Takahashi et al., 2000, 2002; Onodera and Takahashi, 2009). *Neodenticula seminae* is an Alaskan Stream indicator and its abundance in the Bering Sea evidences strong penetration of Alaskan Stream waters through the passes of the Aleutian Islands. By contrast, in glacial-age Bering Sea sediments, the relative abundance of *N. seminae* is typically <10% due to more limited access through the depth-restricted passes at times of lowered sea level. Lower SST in glacial age might also function as a barrier to northern habitat limit of *N. seminae* because the recent common occurrence of *N. seminae* in the Nordic and Labrador Seas has been limited warmer than ~8 °C summer sea-surface temperature (Matul and Kazarina, 2020). In the last deglaciation progressively increasing abundances are seen attaining values consistently >30%

from 8 ka. (Caissie et al., 2010). We therefore use the relative abundance of *N. seminae* together with other diatom indicators to enable environmental reconstruction.

5.2.2. Interval 14H-1, MIS 19

During MIS 20 an ice sheet was present in southwestern Alaska with extensive ice also fringing the Aleutian Basin on the Koryak mountains (Batchelor et al., 2019) and there is biomarker (IP_{25}) evidence for sea ice presence over the Bowers Ridge (Detlef et al., 2018). In the earliest part of the lower laminated interval the intermittent occurrence of *Thalassiosira antarctica* resting spores (up to 38%) and *Fragilariopsis oceanica* and *F. cylindrus* with abundances of 10–15% suggests the influence of a winter sea-ice margin (Figs. 3g; 6, 8f). Based on the modern biogeographic relationship between % *F. oceanica* + *F. cylindrus* in surface sediments and distance from the winter ice margin (Ren et al., 2014), this would put the contemporaneous sea ice margin within 500 km of the site (Fig. 1a) before rapidly receding thereafter. Just before the start of the lower laminated section, common occurrences of *Rhizosolenia* and *Proboscia* which are adapted to stratified waters (Kemp et al., 2000) are consistent with the input of meltwater (Fig. 6). The changes in diatom relative abundance in this interval fit the transition from glacial to interglacial, with abundances of *N. seminae* increasing from 10 to 30% in the lower section to 30–80% in the upper part evidencing increased penetration of Alaskan Stream waters concomitant with rising sea level and the possible decrease of shelf water advection (Fig. 6). This suggests that this interval progresses well into the termination.

Intermittent, elevated abundances (10–30%) of *Paralia sulcata* also occur in the lower laminated interval. *Paralia sulcata* is rare in the modern diatom flora on the Bowers Ridge (station AB, Onodera and Takahashi, 2009) but is common in the world's shallow seas including the modern Bering Sea shelf (Sancetta, 1982; Lopes and Mix, 2018) as it has tychopelagic ecology. In keeping with the interpretation of Cassie et al. (2016) for the MIS 11 sediments at Site U1345, this may indicate lateral input of shelf waters. The analyzed REE compositions (Eu/Eu* of ~0.95 and LREE/HREE of 1.97 to 4.61) suggest that much of lithogenic materials were also transported from the southern shelf side of the Bering Sea and the Aleutian Islands. This source is consistent with the mineralogy of the coarser lithogenic sediment that include altered igneous grains (Fig. 7).

Although the time span of the homogenous interval separating the two laminated sections is uncertain, its duration might be ~165 years based on the age model from the studied core sections. Similar to the diatom assemblage in the initial part of the lower laminated interval, the upper laminated interval contains initial higher abundances of *Rhizosolenia* group and *Actinocyclus curvulatus* (Fig. 6g) suggesting stratified surface waters prior to the onset of lamina preservation. The elevated abundances of *N. seminae* (30–80%) in the upper laminated interval indicates increased influence of the Alaskan Stream and this is consistent with Eu/Eu* values (~1.0) of REE (Fig. 9) that also suggest the intensified input of North Pacific waters via the Aleutian passes. Negligible amounts of *P. sulcata* demonstrate reduced input from shelf waters. The reduced abundance of *Chaetoeros* resting spores in the upper interval is consistent with reduced coastal influence to be expected with increasing sea level.

5.2.3. Interval 10H-1, 2 early MIS 13

Smear slide samples were not taken for the lower laminated interval but estimates from diatoms counted from BSEI were made (Fig. 8c). In the first 30 years abundant *Thalassiothrix* and low abundance of *N. seminae* suggests stratified surface waters with minor input of Pacific water from the Aleutian passes. Thereafter, increased abundance of *N. seminae* evidences stronger influence of Alaskan Stream waters. While *Thalassiothrix* may be characteristic of stratified surface waters, its mass sedimentation often occurs at frontal zones (Kemp et al., 2006). Other diatom-based palaeoceanographic studies of the Bowers Ridge on glacial-interglacial time scales propose the existence of a frontal zone between the seasonal sea ice zone and the open waters (Katsuki and Takahashi, 2005; Stroynowski et al., 2015), so it may be that such a frontal zone promoted the mass flux of *Thalassiothrix* observed here.

In the upper part of this interval (Fig. 6c), there is a marked reduction in the relative abundance of *N. seminae*, indicating decreased influence of the Alaskan Stream. There is also a concomitant increase in the sea ice indicators *Fragilariopsis oceanica* and *F. cylindrus*, to values of around 10%, suggesting the presence of a sea ice margin <500 km from the site. There is also an increase in the occurrence of thicker lithogenic laminae in this interval, testifying to increased rafting of turbid ice. These indicators are consistent with further cooling during this episode, with lowering sea levels and/or increased shelf water advection around the Bowers Ridge leading to reduced penetration of Alaska Stream waters. The 20–30 year periodicities in *Thalassiothrix* and *Neodenticula* abundance discussed above, likely represent intervals where a strengthened Alaskan Stream was better able to penetrate to the Bering Sea.

This interval is within a period where there is no pebble-sized IRD present in IODP Expedition 323 sites from the Bering Sea shelf (Dadd and Foley, 2016), and we find no particles coarser than 250-μm, suggesting the absence of rafting of glacial or fast ice. Nevertheless, the thick lithogenic laminae and REE provenance data that we find attest to recurrent rafting of turbid ice from either or both of the Aleutian Islands and the shallower regions of eastern Bering Sea Shelf through this interval.

At the same time as the cooling, there is an increase in the abundance of *Chaetoceros* spp. resting spores attesting to high productivity. The occurrence of *Odontella*, a neritic taxon, present in the modern, on or near the Bering shelf (Sancetta, 1982) together with the presence of *Paralia sulcata* evidence increased shelf influence with lowering sea levels. The evidence of high productivity is consistent with evidence from the northernmost Bowers Ridge at this time, where benthic foraminifera assemblages from site U1342 show high productivity during the early MIS 13 (Kender et al., 2019). The overall polarity of change within this interval with initial warming and cooling at the top is consistent with the initial warming followed by centennial-millenienial scale cooling in the early part of MIS 13 (Fig. 1).

One key difference with the 14H flora is the greater abundance of *Shionodiscus trifultus*, typically consistently between 10 and 30% in the 10H sequence, but generally <5% in 14H. *Shionodiscus trifultus* is an indicator of summer stratification (Sancetta, 1983), that may be enhanced by the presence of a dicothermal layer (Cassie et al., 2016). This suggests that the less warm, 10H interval, was characterized by more intense summer stratification, possibly enhanced by meltwater input. The greater abundance of *Coscinodiscus* spp. as well as of *Rhizosolenia* and *Proboscia* (Fig. 6c), all "Fall Dump" taxa (Kemp et al., 2000) further suggests elevated late season productivity in the stratified waters.

6. Conclusions

Laminated sediments from the Bowers Ridge of the Bering Sea have been examined using a combination of conventional micropaleontological methods with scanning electron microscope analysis. The analyzed intervals dated from ~528 ka, corresponding to early MIS 13, and ~ 782 ka to early MIS 19. Diatom indicators suggest that the site was likely within 500 km of an ice margin only in the earliest and later part of the MIS 13 laminated interval and in the earliest part of the MIS19 interval consistent with the inferred polarity of climate change in this intervals. There is no lithogenic material larger than fine sand in size indicating an absence of rafting of glacial or fast ice during both intervals, but there is recurrent evidence for regular rafting of turbid ice. Productivity was high in both intervals with total mass fluxes around 5 times higher than modern values supporting current views that lamina preservation in Bering Sea sediments was due to increased productivity, organic matter flux and resulting depletion of oxygen in bottom waters. Input of lithogenic matter was abundant compared to the today's level,

and the origin of lithogenic matter was the southern shelf of the Bering Sea and the Aleutian Arc.

Detailed analysis of SEM images enables a paleo-sediment trap reconstruction of flux events and reveals the seasonal cycle of diatom productivity and lithogenic flux. Early season spring blooms are represented by the resting spores of *Chaetoceros* spp. and more rarely, *Thalassiosira antarctica*. The main spring and summer blooms comprise, often near monospecific, concentrations of vegetative cells of *Shionodiscus trifultus*, *Thalassiosira* spp., *Actinocyclus curvulatus*, and *Neodenticula seminae*. Elevated concentrations of *S. trifultus* likely indicated episodes of enhanced stratification, while increased abundances of *N. seminae* indicate enhanced input from the North Pacific Alaskan Stream during times of reduced land ice and elevated sea level. High abundances of the stratified-adapted *Coscinodiscus* spp. in the uppermost part of the diatom laminae evidences the action of autumn storms that break down stratification resulting in mass sedimentation in the "Fall Dump" of diatoms. Some lithogenic material may co-occur with the *Coscinodiscus* spp. indicating contemporaneous sediment suspension. Indeed, the action of autumn or early winter storms is also indicated by the presence of the coarse silt to fine sand component (40–250 μm) in the lithogenic laminae. This size fraction, with a cut off above fine sand, uniquely indicates rafting of turbid ice that results from the uplift of lithogenic particles by frazil ice in turbulent super-cooled waters. Much of the finer clay and silt fraction was likely input from hemipelagic suspensions arising from river input and conventional storm activity.

Some distinct periodicities occur in lamina thickness variation and in diatom occurrence. The strongest and most persistent periodicities in the 20–30 year band likely represent the influence of the Pacific Decadal Oscillation on strengthening the Alaskan Stream and driving increased penetration of warmer waters to the Bering Sea. The cyclicity in the quasibiennial and 4–8 year bands in may reflect an influence of climate variability driven by El Nino events. Variability in diatom floras also suggests a decadal-scale variability in the intensity of stratification and frontal zone activity.

CRediT authorship contribution statement

Jonaotaro Onodera: Conceptualization, Investigation, Writing – original draft, Writing – review & editing. **Alan E.S. Kemp:** Conceptualization, Investigation, Writing – original draft, Writing – review & editing. **Richard B. Pearce:** Investigation, Writing – original draft. **Keiji Horikawa:** Conceptualization, Investigation, Writing – original draft, Writing – review & editing. **Kozo Takahashi:** Conceptualization, Investigation, Writing – original draft.

Declaration of Competing Interest

Jonaotaro Onodera reports financial support was provided by Japan Society for the Promotion of Science. Keiji Horikawa reports financial support was provided by Japan Society for the Promotion of Science.

Data availability

The dataset on the studied laminated sediment is available from the PANGAEA (Onodera et al., 2023, https://doi.pangaea.de/10.1594/PANGAEA.963903). The dataset on the modern sinking particle flux (Takahashi et al., 2012b) is available at: https://ads.nipr.ac.jp/data/meta/A20230725-001 in the Arctic Data archive System, Japan.

Acknowledgements

This research used sediment core samples and data provided by the Integrated Ocean Drilling Program (IODP). We thank all the captain and crew of D/V JOIDES Resolution and IODP staff for the successful drilling expedition and sampling. We are grateful to all of Expedition 323 Scientists including Dr. Christina A. Ravelo (co-chief scientist), and Dr. Carlos A. Zarikian (staff scientist). This study was partially supported by JSPS Research Fellowships for Young Scientists no. 22-5808 to J.O., and JSPS KAKENHI no. 23810009 to K.H.

Appendix A. Supplementary data

Supplementary data to this article can be found online at https://doi.org/10.1016/j.marmicro.2023.102323.

References

Anders, E., Grevesse, N., 1989. Abundances of the elements: Meteoritic and solar. Geochim. Cosmochim. Acta 53, 197–214.

Asahara, Y., Takeuchi, F., Nagashima, K., Harada, N., Yamamoto, K., Oguri, K., Tadai, O., 2012. Provenance of terrigenous detritus of the surface sediments in the Bering and Chukchi Seas as derived from Sr and Nd isotopes: Implications for recent climate change in the Arctic regions. Deep-Sea Res. II 61-64, 155–171. https://doi.org/10.1016/j.dsr2.2011.12.004.

Asahi, S. Kender, Ikehara, M., Sakamoto, T., Takahashi, K., Ravelo, A.C., Alvarez Zarikian, C.A., Khim, B.K., Leng, M.J., 2016. Orbital-scale benthic foraminiferal oxygen isotope stratigraphy at the northern Bering Sea Slope Site U1343 (IODP Expedition 323) and its Pleistocene paleoceanographic significance. Deep-Sea Res. II 125-126, 66–83. https://doi.org/10.1016/j.dsr2.2014.01.004.

Baroni, I.R., Palastange, V., Slomp, C.P., 2020. Enhanced organic carbon burial in sediments of oxygen minimum zones upon ocean deoxygenation. Front. Mar. Sci. 6, 839. https://doi.org/10.3389/fmars.2019.00839.

Batchelor, C.L., Margold, M., Krapp, M., Murton, D.K., Dalton, A.S., Gibbard, P.L., Stokes, C.R., Murton, J.B., Manica, A., 2019. The configuration of Northern Hemisphere ice sheets through the Quaternary. Nat. Commun. 10, 3713. https://doi.org/10.1038/s41467-019-11601-2.

Brown, Z.W., van Dijken, G.L., Arrigo, K.R., 2011. A reassessment of primary production and environmental change in the Bering Sea. J. Geophys. Res. 116, C08014. https://doi.org/10.1029/2010JC006766.

Caissie, B.E., Brigham-Grette, J., Lawrence, K.T., Herbert, T.D., Cook, M.S., 2010. Last glacial maximum to Holocene sea surface conditions at Umnak Plateau, Bering Sea, as inferred from diatom, alkenone, and stable isotope records. Paleoceanography 25, PA1206. https://doi.org/10.1029/2008PA001671.

Cartapanis, O., Tachkawa, K., Romero, O.E., Bard, E., 2014. Persistent millennial-scale link between Greenland climate and northern Pacific Oxygen Minimum Zone under interglacial conditions. Clim. Past 10, 405–418. https://doi.org/10.5194/cp-10-405-2014.

Cassie, B.E., Brigham-Grette, J., Cook, M.S., Colmenero-Hidalgo, E., 2016. Bering Sea surface water conditions during Marine Isotope Stages 12 to 10 at Navarin Canyon (IODP Site U1345). Clim. Past 12, 1739–1763. https://doi.org/10.5194/cp-12-1739-2016.

Cook, M.S., Keigwin, L.D., Sancetta, C.A., 2005. The deglacial history of surface and intermediate water of the Bering Sea. Deep-Sea Res. II 52, 2163–2173. https://doi.org/10.1016/j.dsr2.2005.07.004.

Dadd, K., Foley, K., 2016. A shape and compositional analysis of ice-rafted debris in cores from IODP Expedition 323 in the Bering Sea. Deep-Sea Res. II 125-126, 191–201.

Davis, A., Kemp, A.E.S., Pike, J., 2009. Late Cretaceous seasonal ocean variability from the Arctic. Nature 460, 254–259. https://doi.org/10.1038/nature08141.

Detlef, H., Belt, S.T., Sosdian, S.M., Smik, L., Lear, C.H., Hall, I.R., Cabedo-Sanz, P., Husum, K., Kenser, S., 2018. Sea ice dynamics across the Mid-Pleistocene transition in the Bering Sea. Nat. Commun. 9, 941. https://doi.org/10.1038/s41467-018-02845-5.

Expedition 323 Scientists, 2011. Site U1340. In: Takahashi, K., Ravelo, A.C., Alvarez Zarikian, C.A. (Eds.), The Expedition 323 Scientists, Proc. IODP, 323. Integrated Ocean Drilling Program Management International, Inc., Tokyo https://doi.org/10.2204/iodp.proc.323.104.2011.

Garcia, H.E., Locarnini, R.A., Boyer, T.P., Antonov, J.I., Baranova, O.K., Zweng, M.M., Reagan, J.R., Johnson, D.R., 2014. In: Levitus, S., A. Mishonov Technical Ed (Eds.), World Ocean Atlas 2013, Volume 3: Dissolved Oxygen, Apparent Oxygen Utilization, and Oxygen Saturation, 75. NOAA Atlas NESDIS (27 pp).

Gedalof, Z., Mantua, N.J., Peterson, D.L., 2002. A multi-century perspective of variability in the Pacific Decadal Oscillation: new insights from tree rings and coral. Geophys. Res. Lett. 29, 2204. https://doi.org/10.1029/2002GL015824.

Hebbeln, D., 2000. Flux of ice-rafted detritus from sea ice in the Fram Strait. Deep-Sea Res. II 47, 1773–1790.

Horikawa, K., Martin, E.E., Basak, C., Onodera, J., Seki, O., Sakamoto, T., Ikehara, M., Sakai, S., Kawamura, K., 2015. Pliocene cooling enhanced by flow of low-salinity Bering Sea water to the Arctic Ocean. Nat. Commun. 6, 7587. https://doi.org/10.1038/ncomms8587.

Katsuki, K., Takahashi, K., 2005. Diatoms as paleoenvironmental proxies for seasonal productivity, sea-ice and surface circulation in the Bering Sea during the late Quaternary. Deep-Sea Res. II 52, 2110–2130. https://doi.org/10.1016/j.dsr2.2005.07.001.

Katsuki, K., Itaki, T., Khim, B.K., Uchida, M., Tada, R., 2014. Response of the Bering Sea to 11-year solar irradiance cycles during the Bølling-Allerød. Geophys. Res. Lett. 41, 2892–2898.

Kemp, A.E.S., Pike, J., Pearce, R.B., Lange, C.B., 2000. The "Fall dump" - a new perspective on the role of a "shade flora" in the annual cycle of diatom production and export flux. Deep-Sea Res. Part II Top. Stud. Oceanogr. 47, 2129–2154.
Kemp, A.E.S., Pearce, R.B., Grigorov, I., Rance, J., Lange, C.B., Quilty, P., Salter, I., 2006. Production of giant marine diatoms and their export at oceanic frontal zones: Implications for Si and C flux from stratified oceans. Glob. Biogeochem. Cycles 20, GB4S04. https://doi.org/10.1029/2006GB002698.
Kempema, E.W., Reimnitz, E., Barnes, P.W., 1989. Sea ice sediment entrainment and rafting in the Arctic. J. Sediment. Petrol. 59, 308–317.
Kender, S., Ravelo, A.C., Worne, S., Swann, G.E.A., Leng, M.J., Asahi, H., Becker, J., Detlef, H., Aiello, I.W., Andreasen, D., Hall, I.R., 2018. Closure of the bering strait caused mid-pleistocene transition cooling. Nat. Commun. 9, 5386. https://doi.org/10.1038/s41467-018-07828-0.
Kender, S., Aturamu, A., Zalasiewicz, J., Kaminski, M.A., Williams, M., 2019. Benthic foraminifera indicate Glacial North Pacific Intermediate Water and reduced primary productivity over Bowers Ridge, Bering Sea, since the Mid-Brunhes transition. J. Micropalaeontol. 38, 177–187. https://doi.org/10.5194/jm-38-177-2019.
Knudson, K.P., Ravelo, A.C., 2015. North Pacific Intermediate Water circulation enhanced by the closure of the Bering Strait. Paleoceanography 30, 1287–1304. https://doi.org/10.1002/2015PA002840.
Knudson, K.P., Ravelo, A.C., Aiello, I.W., Knudson, C.P., Drake, M.K., Sakamoto, T., 2021. Causes and timing of recurring subarctic Pacific hypoxia. Sci. Adv. 7, eabg2906.
Krawczyk, D.W., Witkowski, A., Wroniecki, M., Waniek, J., Kurzydlowski, K.J., Plocinski, T., 2012. Reinterpretation of two diatom species from the West Greenland margin - *Thalassiosira kushirensis* and *Thalassiosira antarctica* var. *borealis* - hydrological consequences. Mar. Micropaleontol. 88-89, 1–14. https://doi.org/10.1016/j.marmicro.2012.02.004.
Kuehn, H., Lembke-Jene, L., Gersonde, R., Esper, O., Lamy, F., Arz, H., Kuhn, G., Tiedemann, R., 2014. Laminated sediments in the Bering Sea reveal atmospheric teleconnections to Greenland climate on millennial to decadal timescales during the last deglaciation. Clim. Past 10, 2215–2236. https://doi.org/10.5194/cp-10-2215-2014.
Lisiecki, L.E., Raymo, M.E., 2005. A Pliocene-Pleistocene stack of 57 globally distributed benthic d18O records. Paleoceanography 20, PA1003. https://doi.org/10.1029/2004PA001071.
Lopes, C., Mix, A.J., 2018. North pacific paleotemperature and paleoproductivity reconstructions based on diatom species. Paleoceanogr. Paleoclimatol. 33, 703–715. https://doi.org/10.1029/2018PA003352.
Lund, S., Stoner, J., Okada, M., Mortazavi, E., 2016. Paleomagnetic field variability and chronostratigraphy of Brunhes-Chron deep-sea sediments from the Bering Sea: IODP Expedition 323. Deep-Sea Res. II 125–126, 107–116. https://doi.org/10.1016/j.dsr2.2016.02.004.
Matul, A., Kazarina, G.K., 2020. The North Pacific diatom species *Neodenticula seminae* in the modern and Holocene sediments of the North Atlantic and Arctic. Geosciences 10, 173. https://doi.org/10.3390/geosciences10050173.
Meese, D.A., Reimnitz, E., Tucker, W.B., Gow, A.J., Bischof, J., Darby, D., 1997. Evidence for radionuclide transport by sea ice. Sci. Total Environ. 202, 267–278.
Mesquita, M.D.S., Atkinson, D.E., Hodges, K.I., 2010. Characteristics and variability of storm tracks in the North Pacific, Bering Sea, and Alaska. J. Clim. 23, 294–311.
Mizobata, K., Saitoh, S.I., Shiomoto, A., Miyamura, T., Shiga, N., Imai, K., Toratani, M., Kajiwara, Y., Sasaoka, K., 2002. Bering Sea cyclonic and anticyclonic eddies observed during summer 2000 and 2001. Prog. Oceanogr. 55, 65–75.
Murdmaa, I.O., Dorokhova, E.V., Ovsepyan, E.A., Dara, O.M., Nurnberg, D., 2019. Terrigenous Sedimentation on the Submarine Shirshov Ridge (Bering Sea) during the Last Deglaciation. Lithol. Miner. Resour. 54, 79–92. https://doi.org/10.1134/S0024490219020068.
Okazaki, Y., Timmermann, A., Menviel, L., Harada, N., Abe-Ouchi, A., Chikamoto, M.O., Mouchet, A., Asahi, H., 2010. Deepwater formation in the North Pacific during the last Glacial termination. Science 329, 200. https://doi.org/10.1126/science.1190612.
Onodera, J., Takahashi, K., 2009. Long-term diatom fluxes in response to oceanographic conditions at Stations AB and SA in the central subarctic Pacific and the Bering Sea, 1990-1998. Deep-Sea Research I 56, 189–211. https://doi.org/10.1016/j.dsr.2008.08.006.
Onodera, J., Kemp, A.E.S., Pearce, R., Horikawa, K., Takahashi, K., 2023. Lamina Thickness, Diatom Assemblage, and Rare-Earth Element Composition in the Varved Sediments of the Mid-Pleistocene Bering Sea (Cores IODP Expedition 323-U1340A-10H and 14H). PANGAEA. https://doi.pangaea.de/10.1594/PANGAEA.963903.
Osafune, S., Masuda, S., Sugiura, N., 2014. Role of the oceanic bridge in linking the 18.6 year modulation of tidal mixing and long-term SST change in the North Pacific. Geophys. Res. Lett. 41, 7284–7290. https://doi.org/10.1002/2014GL061737.
Panteleev, G., Luchin, V., Nezlin, N.P., Kikuchi, T., 2013. Seasonal climatologies of oxygen and phosphates in the Bering Sea reconstructed by variational data assimilation approach. Polar Sci. 7, 214–232. https://doi.org/10.1016/j.polar.2013.10.001.
Pike, J., Kemp, A.E.S., 1996. Preparation and analysis techniques for studies of laminated sediments. Geol. Soc. Spec. Publ. 116, 37–48.
Praetorius, S.K., Mix, A.C., Walczak, M.H., Wolhowe, M.D., Addison, J.A., Prahl, F.G., 2015. North Pacific deglacial hypoxic events linked to abrupt ocean warming. Nature 527, 362–366.
Ren, J., Gersonde, R., Esper, O., Sancetta, C., 2014. Diatom distributions in northern North Pacific surface sediments and their relationships to modern environmental variables. Palaeogeogr. Palaeoclimatol. Palaeoecol. 402, 81–103. https://doi.org/10.1016/j.palaeo.2014.03.008.
Roden, G.I., 1995. Aleutian Basin of the Bering Sea: Thermohaline, oxygen, nutrient, and current structure in July 1993. J. Geophys. Res. 100, 13539–13554.
Roesch, A., Schmidbauer, H., 2018. WaveletComp: Computational Wavelet Analysis. R Package Version 1.1. https://CRAN.R-project.org/package=WaveletComp.
Sancetta, C., 1982. Distribution of diatom species in surface sediments of the Bering and Okhotsk Seas. Micropaleontology 28, 221–257.
Sancetta, C., 1983. Effect of Pleistocene glaciation upon oceanographic characteristics of the North Pacific Ocean and Bering Sea. Deep-Sea Res. 30, 851–869.
Sancetta, C., Heusser, L., Laveyrie, L., Naidu, A.S., Robinson, S.W., 1985. Wisconsin-Holocene paleoenvironment of the Bering Sea: evidence from diatoms, pollen, oxygen isotopes and clay minerals. Mar. Geol. 62, 55–68.
Schimmelmann, A., Lange, C.B., Schieber, J., Francus, P., Ojala, A.E.K., Zolitschka, B., 2016. Varves in marine sediments: a review. Earth Sci. Rev. 159, 215–246. https://doi.org/10.1016/j.earscirev.2016.04.009.
Schlung, S.A., Ravelo, A.C., Aiello, I.W., Andreasen, D.H., Cook, M.S., Drake, M., Dyez, K. A., Guilderson, T.P., LaRiviere, J.P., Stroynowski, Z., Takahashi, K., 2013. Millennial-scale climate change and intermediate water circulation in the Bering Sea from 90ka: a high-resolution record from IODP Site U1340. Paleoceanography 28, 54–67. https://doi.org/10.1029/2012PA002365.
Schmittner, A., Galbraith, E.D., Hostetler, S.W., Pedersen, T.F., Zhang, R., 2007. Large fluctuations of dissolved oxygen in the Indian and Pacific oceans during Dansgaard-Oeschger oscillations caused by variations of North Atlantic Deep Water subduction. Paleoceanography 22.
Seip, K.L., Grøn, Ø., 2019. On the statistical nature of distinct cycles in global warming variables. Clim. Dyn. 52, 7329–7337. https://doi.org/10.1007/s00382-016-3508-6.
Sherwood, C.R., 2000. Numerical model of frazil ice and suspended sediment concentrations and formation of sediment laden ice in the Kara Sea. J. Geophys. Res. Oceans 105, 14061–14080.
Smedsrud, L.H., 2001. Frazil-ice entrainment of sediment: large-tank laboratory experiments. J. Glaciol. 47, 461–471.
Smedsrud, L.H., 2003. Formation of turbid ice during autumn freeze-up in the Kara Sea. Polar Res. 22, 267–286. https://doi.org/10.1111/j.1751-8369.2003.tb00112.x.
Stabeno, P.J., Schumacher, J.D., Ohtani, K., 1999. The physical oceanography of the Bering Sea: a summary of physical, chemical, and biological characteristics, and a synopsis of research on the Bering Sea. In: Loughlin, T.R., Ohtani, K. (Eds.), Dynamics of the Bering Sea. University of Alaska Sea Grant, pp. 1–28.
Stroynowski, Z., Ravelo, A.C., Andreasen, D., 2015. A Pliocene to recent history of the Bering Sea at Site U1340A, IODP Expedition 323. Paleoceanography 30, 1641–1656. https://doi.org/10.1002/2015PA002866.
Takahashi, K., Fujitani, N., Yanada, M., Maita, Y., 2000. Long-term biogenic particle fluxes in the Bering Sea and the central subarctic Pacific Ocean 1990-1995. Deep-Sea Research I 47, 1723–1759.
Takahashi, K., Fujitani, M., Yanada, M., 2002. Long term monitoring of particle fluxes in the Bering Sea and the central subarctic Pacific Ocean, 1990-2000. Prog. Oceanogr. 55, 95–112.
Takahashi, K., Ravelo, A.C., Zlvarez-Zarikian, C.A., the Expedition 323 Scientists, 2011. Bering Sea Paleoceanography. Proc. Integr. Ocean Drilling Prog. 323 https://doi.org/10.2204/iodp.proc.323.2011.
Takahashi, K., Asahi, H., Okazaki, Y., Onodera, J., Tsutsui, H., Ikenoue, T., Kanematsu, Y., Tanaka, S., Iwasaki, S., 2012a. Museum archives of the 19 years long time-series sediment trap samples collected at central subarctic Pacific Station SA and Bering Sea Station AB during 1990-2010. Mem. Faculty Sci. Kyushu Univ. Ser. D Earth Planet. Sci. 32 (4), 1–38.
Takahashi, K., Asahi, H., Okazaki, Y., Onodera, J., Tsutsui, H., Ikenoue, T., Kanematsu, Y., Tanaka, S., Iwasaki, S., 2012b. Updated dataset on the sinking particle fluxes collected at central subarctic Pacific Station SA and Bering Sea Station AB during 1990-2010. Updated dataset on the sinking particle fluxes collected at central subarctic Pacific Station SA and Bering Sea Station AB during 1990-2010, 0.00. Arctic Data archive System (ADS), Japan. https://doi.org/10.17592/001.2023072501.
Tanaka, S., Takahashi, K., 2005. Late Quaternary paleoceanographic changes in the Bering Sea and the western subarctic Pacific based on radiolarian assemblages. Deep-Sea Res. II 52, 2131–2149. https://doi.org/10.1016/j.dsr2.2005.07.002.
Wang, R., Biskaborn, B.K., Ramish, A., Ren, J., Zhang, Y., Gersonde, R., Diekmann, B., 2016. Modern modes of provenance and dispersal of terrigenous sediments in the North Pacific and the Bering Sea: implications and perspectives for palaeoenvironnmental reconstructions. Geo-Mar. Lett. 36, 259–270. https://doi.org/10.1007/s00367-016-0445-7.
Wang, R., Kuhn, G., Gong, X., Biskaborn, B.K., Gersonde, R., Lembke-Jene, L., Lohmann, G., Tiedemann, R., Diekmann, B., 2021. Deglacial land-ocean linkages at the Alaskan Continental Margin in the Bering Sea. Front. Earth Sci. 9, 712415 https://doi.org/10.3389/feart.2021.712415.
Yamamoto, K., Yamashita, F., Adachi, M., 2005. Precise determination of REE for sedimentary reference rocks issued by the Geological Survey of Japan. Geochem. J. 39, 289–297.
Yang, X.-Y., Wang, G., Keenlyside, N., 2020. The Arctic sea ice extent change connected to Pacific decadal variability. Cryosphere 14, 693–708. https://doi.org/10.5194/tc-14-693-2020.